iScience

CellPress

Article

Rapid Turnover of the Cardiac L-Type $Ca_V1.2$ Channel by Endocytic Recycling Regulates Its Cell Surface Availability

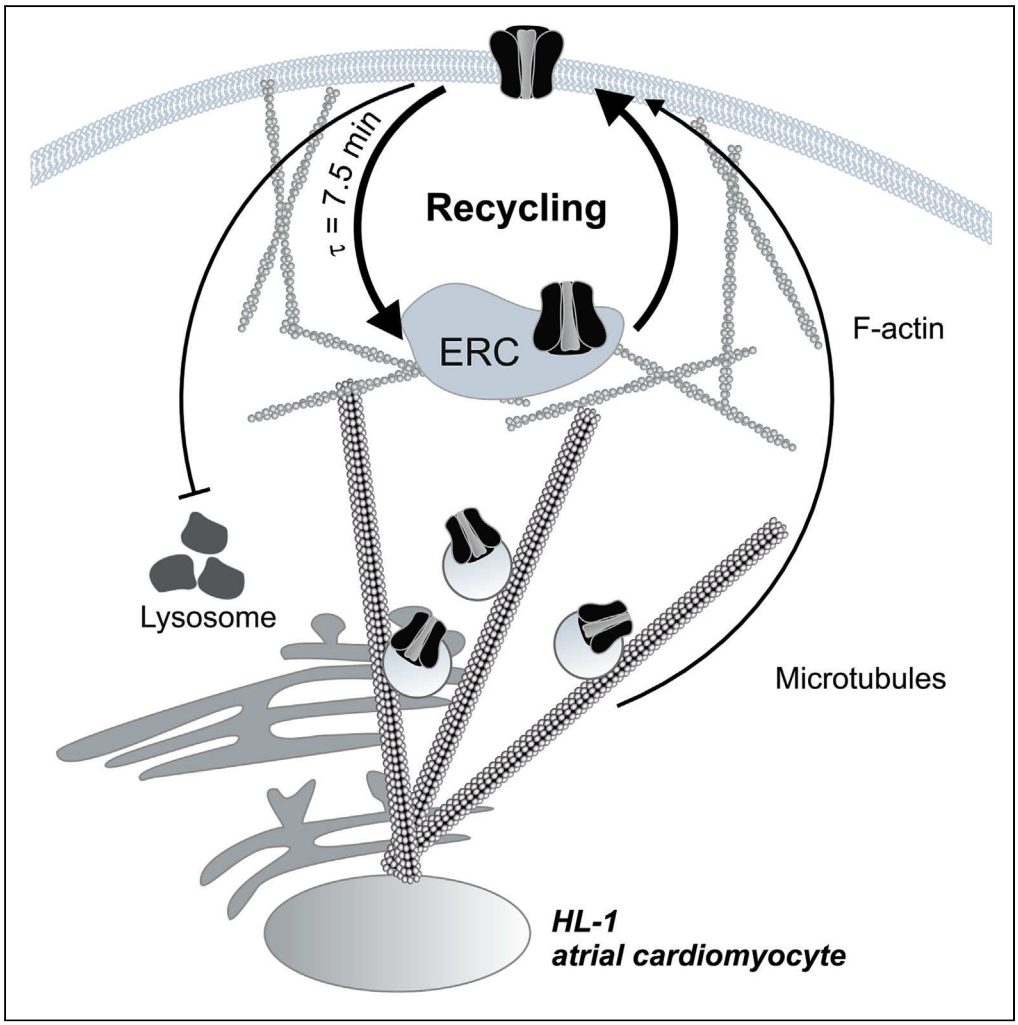

Rachel Conrad, Gabriel Stölting, Johnny Hendriks, ..., Nadine Jordan, Thomas Gensch, Patricia Hidalgo

pa.hidalgo@fz-juelich.de

HIGHLIGHTS

$Ca_V1.2$ channels dwell only about 10 min in the plasma membrane of atrial cells

$Ca_V1.2$ recycles via Rab11a endocytic recycling compartment along actin filaments

Recycling of $Ca_V1.2$ is essential for maintaining stable L-type current amplitudes

Surface $Ca_V1.2$ homeostasis is independent of tubulin-based transport over 20 hr

Conrad et al., iScience 7, 1–15
September 28, 2018
https://doi.org/10.1016/j.isci.2018.08.012

iScience

CellPress

Article

Rapid Turnover of the Cardiac L-Type $Ca_V1.2$ Channel by Endocytic Recycling Regulates Its Cell Surface Availability

Rachel Conrad,[1] Gabriel Stölting,[1] Johnny Hendriks,[1] Giovanna Ruello,[1,3] Daniel Kortzak,[1] Nadine Jordan,[1] Thomas Gensch,[1] and Patricia Hidalgo[1,2,4,*]

SUMMARY

Calcium entry through $Ca_V1.2$ L-type calcium channels regulates cardiac contractility. Here, we study the impact of exocytic and post-endocytic trafficking on cell surface channel abundance in cardiomyocytes. Single-molecule localization and confocal microscopy reveal an intracellular $Ca_V1.2$ pool tightly associated with microtubules from the perinuclear region to the cell periphery, and with actin filaments at the cell cortex. Channels newly inserted into the plasma membrane become internalized with an average time constant of 7.5 min and are sorted out to the Rab11a-recycling compartment. $Ca_V1.2$ recycling suffices for maintaining stable L-type current amplitudes over 20 hr independent of *de novo* channel transport along microtubules. Disruption of the actin cytoskeleton re-routes $Ca_V1.2$ from recycling toward lysosomal degradation. We identify endocytic recycling as essential for the homeostatic regulation of voltage-dependent calcium influx into cardiomyocytes. This mechanism provides the basis for a dynamic adjustment of the channel's surface availability and thus, of heart's contraction.

INTRODUCTION

Depolarization of cardiomyocytes opens $Ca_V1.2$ L-type voltage-activated calcium channels, allowing the influx of calcium ions, which in turn triggers calcium release from the sarcoplasmic reticulum, permitting effective myofilament contraction (Bodi et al., 2005). The $Ca_V1.2$ core complex is composed of the $Ca_V1.2$ α_1 ion-conducting subunit, plus the accessory $\alpha_2\delta$- and β-subunits that regulate the conduction properties and surface expression of the channel (Hofmann et al., 2014). The $Ca_V1.2$ α_1 and $Ca_V\beta_2$ subunits are essential for cardiac function. Mice bearing homozygous deletions of either gene die at embryonic stages (Larsen et al., 2002; Link et al., 2009; Rusconi et al., 2016; Seisenberger et al., 2000; Weissgerber et al., 2006). In humans, aberrant calcium permeation through $Ca_V1.2$ channels is associated with several pathological cardiac conditions (Basheer and Shaw, 2016; Dick et al., 2016; Hofmann et al., 2014; Hong et al., 2012; Shaw and Colecraft, 2013; Splawski et al., 2004, 2005). The function and number of channels at the plasma membrane regulates the amount of calcium entering into the cardiomyocytes. The cell surface abundance of $Ca_V1.2$ is determined by the balance between the anterograde traffic that inserts channels into the plasma membrane via the secretory and the recycling pathways and the retrograde traffic that removes channels from the cell surface by endocytosis. The post-endocytic fate towards recycling or degradation can critically affect channel availability, but the extent to which these different trafficking events contribute to calcium current control is poorly understood.

Defective trafficking of the cardiac $Ca_V1.2$ channel protein has been linked to disorders including atrial fibrillation, heart failure, and Brugada syndrome (Antzelevitch et al., 2007; Basheer and Shaw, 2016; Schotten et al., 2003; Simms and Zamponi, 2012; Xiao and Shaw, 2015). Thus, elucidation of the pathway by which $Ca_V1.2$ traffics to and from the plasma membrane is very relevant to understanding heart function and dysfunction.

As for all membrane proteins, ion channels are incorporated into vesicles and directionally transported by motor proteins along two main cytoskeletal tracks, actin and tubulin filaments (Figure 1A). Classically, the microtubule network is considered the major pathway sustaining long-range intracellular vesicular transport, whereas actin filaments are involved in short-range transport processes at the cell cortex. However, long-range vesicle transport mediated by the actin cytoskeleton has been reported (Schuh, 2011). In

[1]Institute of Complex Systems 4, Zelluläre Biophysik, Forschungszentrum Jülich, 52425 Jülich, Germany

[2]Institute of Biochemistry, Heinrich-Heine University, Düsseldorf, Germany

[3]Present address: Department of Physics and Earth Science, University of Messina, 98122 Messina, Italy

[4]Lead Contact

*Correspondence: pa.hidalgo@fz-juelich.de

https://doi.org/10.1016/j.isci.2018.08.012

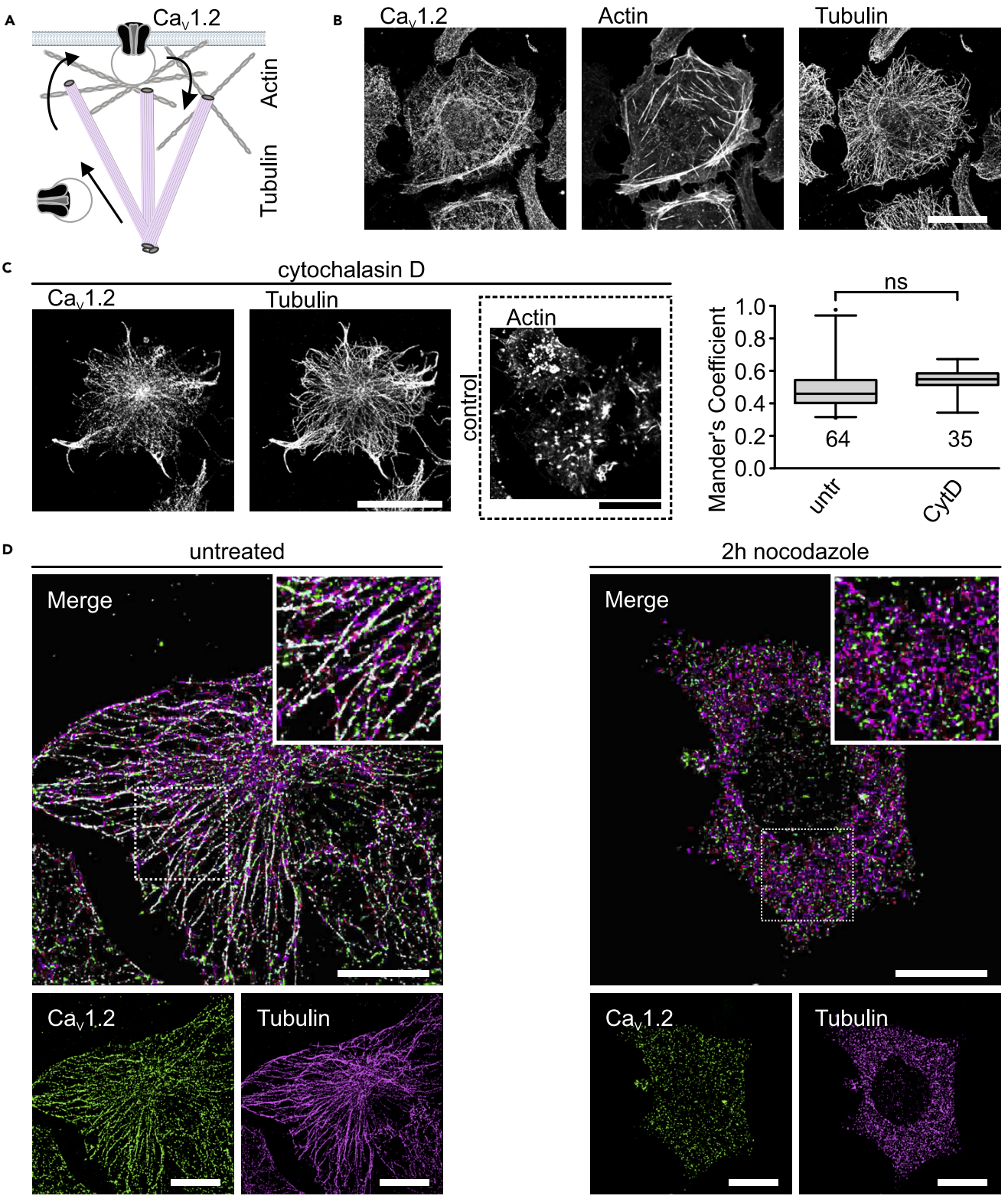

Figure 1. $Ca_V1.2$ Distributes along Microtubules Extending from the Perinuclear Region to the Cell Periphery Independent of an Intact Actin Cytoskeleton

(A) Schema of the intracellular anterograde and retrograde trafficking of the calcium channel. The channel is packed into vesicles that walks along tubulin and actin filaments to be delivered to the plasma membrane from where it can be removed by endocytosis during retrograde traffic.

Figure 1. *Continued*

(B) Laser scanning confocal images of representative HL-1 cells fluorescently stained for $Ca_V1.2$, tubulin and actin, using antibody coupled to ATTO 488, antibody coupled to Cy3 and phalloidin coupled to Alexa Fluor 647, respectively. Scale bar: 25 μm.

(C) Laser scanning confocal images of HL-1 cells immunostained for $Ca_V1.2$ and tubulin in the presence of 10 μM of the actin filament disrupter cytochalasin D and box plot summarizing the colocalization analysis between $Ca_V1.2$ and tubulin according to Manders overlap coefficient in untreated and cytochalasin D treated HL-1 cells. The right panel shows a control cell exposed to the same cytochalasin D treatment and stained for actin using phalloidin-647. Scale bar: 25 μm. Numbers below each box correspond to the number of cells analyzed (*n* size). Each box represents the interquartile range (25^{th} and 75^{th} quartile) with the median indicated by the line. Whiskers above and below indicate the 95% confidence interval. Outliers are shown by dots. Statistical significance (one-way ANOVA, $p \leq 0.001$).

(D) Single-molecule localization microscopy images from representative HL-1 cells immunostained for $Ca_V1.2$ (green) and tubulin (magenta) under normal conditions (left panel) and after 2 hr exposure to the microtubule disrupter nocodazole (right panel). The merged images are shown with an enlarged view of the marked square regions. Overlapping pixels appear in white. Single-molecule localizations were extracted from the data using SNSMIL (Tang et al., 2015). Scale bar: 10 μm for the bottom panels and 1 μm for the merge figure.

cardiomyocytes, $Ca_V1.2$ appears to be transported along microtubule tracks from early secretory compartments to the cell periphery. Here, the scaffolding protein BIN 1 is responsible for delivering the channel to the T-tubules (Hong et al., 2010). In addition, it has been demonstrated that actin filaments play a role in promoting cell surface insertion of $Ca_V1.2$ channels, in atrial-derived HL-1 cells, via their direct association with the β-subunit (Stölting et al., 2015).

Much less is known about the endocytic route of $Ca_V1.2$, although increasing evidence shows that internalization and degradation contribute to regulation of the $Ca_V1.2$ cell surface expression (Best et al., 2011; Catalucci et al., 2009; Felix and Weiss, 2017; Green et al., 2007). Endocytosis and recycling are relatively fast (with half-time values around a couple of minutes [Maxfield and McGraw, 2004]), dynamic, and spatially confined trafficking events that may reversibly switch on and off the channel's cell surface availability, but the relevance of the endocytic pathway in modulating $Ca_V1.2$ cell surface density in cardiac cells has not yet been established.

We investigated the trafficking of $Ca_V1.2$ channels in HL-1 atrial cells. Our findings demonstrate that post-endocytic sorting is essential for governing $Ca_V1.2$ surface availability, challenging the notion that microtubule-mediated transport is the rate-limiting step for maintaining stable $Ca_V1.2$ currents (Hong et al., 2010). Paradoxically, we found that the channel turnover at the plasma membrane is relatively fast, with a time constant of internalization of about 7.5 min. We show that the loss of cell surface channels due to dynamic endocytosis is balanced by reinsertion of recycled channels, rather than of *de novo* synthesized protein, via a pathway mediated by Rab11a. This pathway is dependent on an intact actin cytoskeleton.

Our results may help to develop new strategies for treating $Ca_V1.2$-associated channelopathies aimed at adjusting the number of expressed channels.

RESULTS

Endogenous $Ca_V1.2$ Localizes Along Radially Distributed Microtubules and Peripheral Actin Filaments in HL-1 Cells

We used three-color laser scanning confocal fluorescence microscopy to visualize the distribution of $Ca_V1.2$ channels with respect to the actin- and tubulin-based cytoskeleton in HL-1 cells (Figure 1B). Immunostained $Ca_V1.2$ forms distinct thread-like structures broadly distributed throughout the cell, extending from the perinuclear region to the cell cortex, with prominent accumulation at the cell periphery (Figure 1B, left panel). At periphery, immunostained $Ca_V1.2$ appears to colocalize with phalloidin-stained actin filaments (Figure 1B, middle panel) probably reflecting the association of the channel complex and F-actin via the β-subunit, as previously reported in HL-1 cells (Stölting et al., 2015).

$Ca_V1.2$ thread-like structures at the cell interior closely resemble the distribution of the microtubule network (Figure 1B, right panel). Quantitative analysis of the degree of colocalization between fluorescently labeled $Ca_V1.2$ and microtubules from the confocal laser-scanning images, using Manders' overlap coefficient (MOC) (Bolte and Cordelieres, 2006), resulted in a moderate correlation value (0.49 ± 0.02, Figure 1C). This MOC value is not altered after treating the cells with 10 μM cytochalasin D, which effectively disrupts actin filaments (Figure 1C). This suggests that the delivery of $Ca_V1.2$ to microtubule tracks does not require an intact actin-based cytoskeleton.

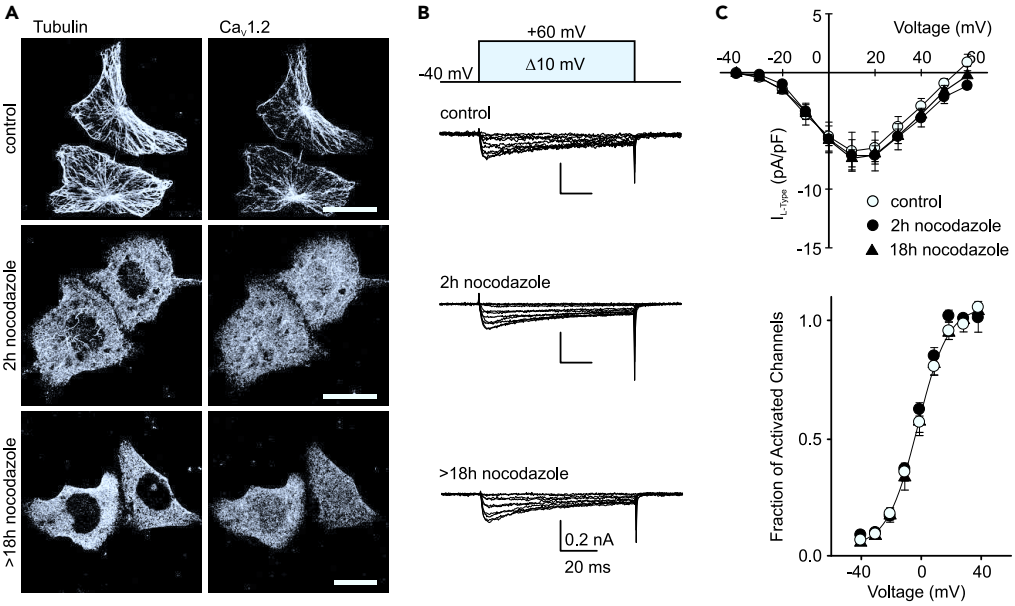

Figure 2. Long-term Stable Expression of L-type Currents in HL-1 Cells Is Independent of Microtubule-Based Transport

(A) Laser scanning confocal images of control HL-1 cells immunostained for tubulin and $Ca_V1.2$ (top panels) or cells following incubation with 33 μM of nocodazole for 2 hr (middle panels) or 18–22 hr (bottom panels). Scale bar: 25 μm.

(B) Representative L-type current traces from cells under the three conditions shown in *A* elicited by voltage steps from a holding potential of −40 mV to +60 mV in 10 mV increments (protocol pulse indicated above).

(C) Average current density to voltage (I-V) curves (upper panel) and fraction of activated channels versus voltage plot (activation curves, lower panel) for L-type currents ($I_{L\text{-}type}$) from different cells as shown in *B* (n = 5 for control cells and n = 6 and 5, for cells exposed to nocodazole for 2 hr and >18 hr, respectively). The continuous line represents the fit to a Boltzmann function for the control dataset.

To study the spatial correlation between $Ca_V1.2$ and tubulin at nanoscale resolution, we used single-molecule localization microscopy (SMLM) on immunofluorescently stained HL-1 cells, as previously described (Stölting et al., 2015). SMLM images from HL-1 cells immunolabeled for $Ca_V1.2$ and tubulin show that $Ca_V1.2$ distributes along microtubules over several micrometers, from the microtubule-organizing center adjacent to the nucleus to the cell periphery (Figure 1D). Pharmacological disruption of the microtubule network using nocodazole resulted in a spotty distribution of $Ca_V1.2$ and tubulin and a loss of the spatial correlation between the channel protein and unpolymerized tubulin subunits (Figure 1D).

Altogether, these results indicate that transport of $Ca_V1.2$ from the early secretory compartments towards the cell periphery takes place along microtubules, and independently of actin filaments. Moreover, they show that a major fraction of the intracellular $Ca_V1.2$ pool associates with cytoskeletal tracks, indicating a role for trafficking processes in regulating channel availability.

Pharmacological Disruption of the Microtubule Network Preserves Endogenous L-type Current Expression in HL-1 Cells

Next, we examined the extent to which microtubule-dependent transport participates in the modulation of $Ca_V1.2$ cell surface expression using the whole-cell patch-clamp technique. L-type currents were recorded from control HL-1 cells and from cells treated with nocodazole for either 2 or 18 hr (Figure 2). The efficacy of nocodazole treatment over the different durations was evaluated by double immunofluorescence labeling of tubulin and $Ca_V1.2$ (Figure 2A). Confocal images show that after 2 hr of exposure to nocodazole the microtubule network is almost fully disrupted, and following 18 hr of treatment, virtually no filaments are visible. In addition, since prolonged nocodazole treatment may lead to Golgi scattering and thus artificial delivery of the channel from endoplasmic reticulum (ER)-Golgi to the plasma membrane (Cole et al., 1996), we also investigated the architecture of the Golgi compartment in cells exposed to the same nocodazole regime as for the electrophysiological recordings. Cells immunostained with a trans-Golgi antibody showed the typical Golgi ribbon structure localized in the perinuclear region (Figure S1). After 2 hr

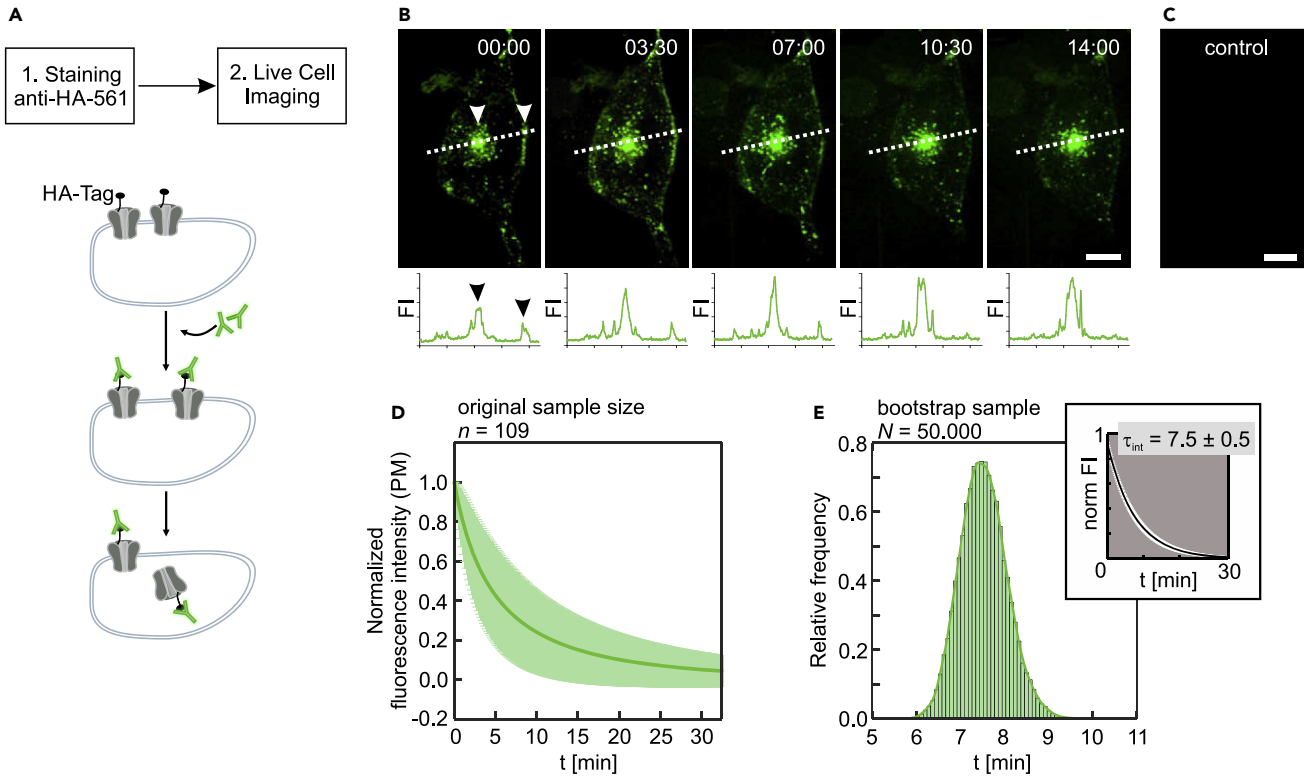

Figure 3. Internalization of $Ca_V1.2$ Channels in HL-1 Cells Occurs within a Few Minutes

(A) Experimental design to follow the time course of $Ca_V1.2$ internalization. HL-1 cells expressing extracellularly HA-epitope tagged $Ca_V1.2$ are incubated with fluorescently labeled anti-HA-antibody at room temperature, washed, and immediately transferred to the cell microscope stage top incubator set at 37°C for live cell imaging using the spinning disk confocal microscopy.

(B) Representative time-lapse image sequence of the course of internalization of fluorescently labeled $Ca_V1.2$ in HL-1 cells. The time after completion of the labeling reaction at which each frame was acquired is indicated. The corresponding fluorescence intensity plots along the dotted line drawn by eye across the middle of the cell are shown in the lower panels. The white arrowheads in the image shown at t = 0 indicate HA-labeled channels accumulated at the cell center and at the plasma membrane and correspond to the black arrowheads in the fluorescence intensity profile shown below. Over time the fluorescence intensity in the plasma membrane decreases, whereas the fluorescence intensity in the inner part of the cell increases. Scale bar: 10 μm.

(C) Non-transfected control HL-1 cells show no HA-mediated signal after incubation with the fluorescently labeled anti-HA tag antibody. Scale bar: 10 μm.

(D) Mean time course of $Ca_V1.2$ internalization (continuous dark green line) and SD (light green shaded area) of all the individual normalized exponential fits to the fluorescence decay of the different regions of interest at the plasma membrane (PM) from different cells analyzed (original sample size n = 109).

(E) Distribution of the time constants obtained from the bootstrap samples. The mean time constant ± SD of internalization (τ_{int}) and confidence interval (CI) extracted from the bootstrap distribution is 7.5 ± 0.5 min with 95% CI from 6.55 to 8.65 min. The insert shows the mean time course of $Ca_V1.2$ internalization (black line) and SD (white shaded area) of the individual exponential fits to all the bootstrap samples (bootstrap sample N = 50,000).

exposure to nocodazole, the cells showed a relatively less compacted juxtanuclear Golgi structure, and after 18 hr of treatment significantly more scattered fragments were observed throughout the cell (Figure S1). Despite the progressive increase in Golgi fragmentation over time of exposure, the L-type current density amplitudes and voltage dependence of activation were preserved (Figures 2B and 2C). Thus, Golgi scattering does not correlate with an increase in L-type currents. Both groups of treated HL-1 cells (for 2 and >18 hr) showed identical current amplitudes and voltage dependence as control cells demonstrating that nocodazole treatment has no effect on both the biophysical properties of the $Ca_V1.2$ channel and the number of functional channels assembled at the plasma membrane (Figures 2B and 2C). This lack of effect of nocodazole indicates that either the lifetime of the channel at the plasma membrane is relatively long (>20 hr) or, alternatively, a mechanism independent of microtubule-based transport is responsible for maintaining steady-state levels of cell surface $Ca_V1.2$.

$Ca_V1.2$ Channels Are Internalized with a Time Constant of a Few Minutes in HL-1 Cells

We assessed the average residence time of $Ca_V1.2$ channels at the plasma membrane of HL-1 cells. Cells were transfected with a cDNA construct encoding $Ca_V1.2$ bearing an extracellular hemagglutinin (HA)

epitope ($Ca_V1.2$-HA). To selectively label channels at the cell surface, $Ca_V1.2$-HA-expressing cells were briefly exposed to a fluorophore-conjugated anti-HA antibody, and the time course of subsequent channel internalization was monitored at 37°C using spinning disk confocal microscopy, as shown in Figures 3A–B. The anti-HA-mediated fluorescence signal was found at the plasma membrane and throughout the cytoplasm in small punctuate structures and was concentrated at the cell interior (Figure 3B). The fluorescence intensity plots across a dotted line within the cell, obtained from the image sequence, show that the membrane staining decreases relatively rapidly over time, whereas the intracellular signal steadily increases (Figure 3B, lower panel). Neither membrane staining nor intracellular retention of the antibody was observed in untransfected cells (Figure 3C).

To estimate the lifetime of the channel at the cell surface, the fluorescence intensity in channel clusters at the plasma membrane from different regions of interest, and in several different cells, were plotted as a function of time and fitted individually to a single exponential, as described in the Transparent Methods section. The mean normalized fitted exponential and the SD for all the analyzed regions of interest is shown in Figure 3D. Using the bootstrap method (Efron and Tibshirani, 1993), the mean time constant of internalization (τ_{int}) $\pm$ SD for $Ca_V1.2$ was calculated from the bootstrap sample distribution, obtaining a value for τ_{int} of 7.5 $\pm$ 0.5 min (Figure 3E). To compare the total protein expression levels of $Ca_V1.2$ in transfected and untransfected cells, we calculated the fluorescence intensity of immunolabeled $Ca_V1.2$. We found that $Ca_V1.2$ expression levels are comparable in both cases, and thus, we assume that the calculated time constant holds for endogenous expressed channels (Figure S2).

Since we observed that cell surface levels of $Ca_V1.2$ are preserved for over 20 hr after disruption of the microtubule network, the relatively rapid $Ca_V1.2$ internalization rate predicts the existence of dynamic trafficking events that must replace the internalized channels by newly inserted ones, independent of a competent microtubule-based cytoskeleton.

We used a dual-pulse staining protocol to estimate the rate at which new $Ca_V1.2$ channels are inserted into the plasma membrane (Figure S3). The first pulse saturates all $Ca_V1.2$ present at the cell surface, whereas the second pulse, 20 min later, labels only channels that have been inserted during the time elapsed between the two pulses, i.e., newly inserted channels. We observed a robust staining of $Ca_V1.2$ channels during the second pulse, indicating that a dynamic insertion of new channels into the plasma membrane takes place during a time window of about 20 min. As predicted from the lack of effect of nocodazole treatment on the cell surface expression of $Ca_V1.2$ (Figure 2), the newly inserted channels originate from the recycling rather than from the microtubule-based secretory pathway, as is shown below. Since we do not observe the fluorescence signal returning to the plasma membrane, we assume that the fluorescently labeled antibody dissociates from the channel during the post-endocytic recycling itinerary.

Altogether, the above findings show that the cell surface $Ca_V1.2$ turnover is very dynamic, that it occurs on a relatively short timescale of tens of minutes, and that internalized $Ca_V1.2$ channels are effectively replaced by newly delivered $Ca_V1.2$ protein.

Endogenous $Ca_V1.2$ Is Internalized via Clathrin-Mediated Endocytosis and Diverted to Rab11-Positive Recycling Endosomes but Not to Lysosomes

We next investigated the endosomal transport of endogenously expressed $Ca_V1.2$ in HL-1 cells by quantifying its degree of colocalization with different endosomal markers along the endocytic pathway using the MOC (Figure 4).

Internalization of receptors and ion channels may occur via clathrin-mediated and clathrin-independent endocytosis. After internalization, the protein is transferred to sorting endosomes and, from there, either recycled back to the plasma membrane by the so-called fast or slow recycling or transported via late endosomes to lysosomes for degradation (McMahon and Boucrot, 2011). During slow recycling, mediated by Rab11 GTPases, cargo proteins are first transferred to the endocytic recycling compartment (ERC) before being recycled back to the plasma membrane with a half-life of around 12 min (Hao and Maxfield, 2000). Fast recycling, mediated by Rab4 GTPases, return cargo to the cell surface directly from the sorting endosomes approximately 10 times faster than slow recycling (Hao and Maxfield, 2000; Maxfield and McGraw, 2004).

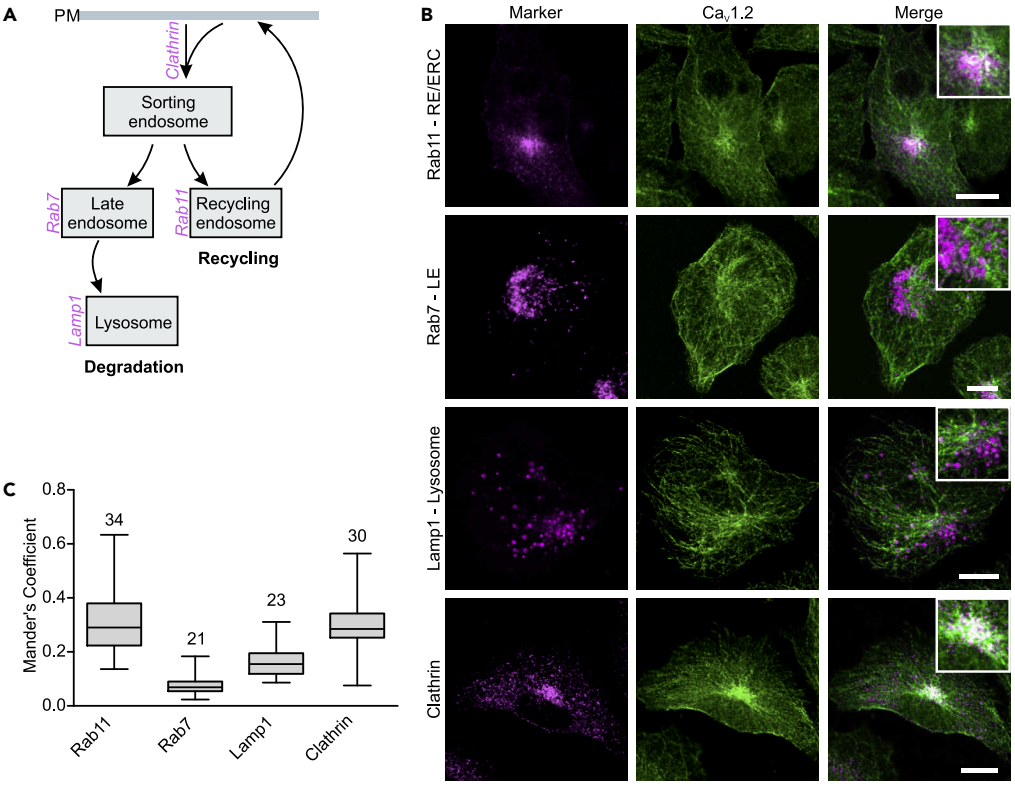

Figure 4. Endogenous $Ca_V1.2$ Colocalizes with Clathrin-Endocytic Vesicles and Rab11a-Recycling Endosomes but Not with Lysosomes

(A) Illustration showing a general endocytic pathway with the endosomal markers used in this study. HL-1 cells were immunostained for $Ca_V1.2$, clathrin, Rab7 (late endosomes, LE), and Rab11a (recycling endosomes and endocytic recycling compartment, RE/ERC). Lysosomes were labeled using a cDNA encoding for LAMP1 fused to monomeric red fluorescent protein (mRFP). PM, plasma membrane.

(B) Laser scanning confocal images of HL-1 cells fluorescently labeled for endogenous $Ca_V1.2$ (green) and the indicated endocytic pathway marker (magenta). The corresponding merge images with an enlarged view are shown at the right. Overlap pixels appear in white. Scale bar: 10 μm.

(C) Box plot summarizing the colocalization analysis between $Ca_V1.2$ and the indicated markers according to Manders' overlap coefficient in HL-1 cells. Numbers above each box represent the number of cells analyzed (*n* size). Each box represents the interquartile range (25^{th} and 75^{th} quartile) with the median indicated by a line. Whiskers above and below indicate the 95% confidence interval. $Ca_V1.2$ colocalizes with clathrin and Rab11-positive endosomes but not with late endosomes (Rab7-positive) or lysosomes (Lamp1).

We analyzed the spatial correlation of $Ca_V1.2$ with clathrin, and also with Rab11a, a marker for recycling endosomes (RE) and the perinuclear ERC, and also of $Ca_V1.2$ with the degradation pathway markers, Rab7 (for late endosomes) and LAMP1 (for lysosomes) (Figure 4A). The laser scanning confocal images show that $Ca_V1.2$ distribution overlaps with that of clathrin and Rab11a, but not with that of Rab7 and Lamp1 (Figures 4B and 4C). The MOC values obtained show a modest, but significantly higher degree of colocalization between $Ca_V1.2$ and either clathrin or Rab11a than is observed between $Ca_V1.2$ and either Rab7-positive late endosomes or lysosomes (Figure 4C).

These results demonstrate that endogenous $Ca_V1.2$ is partly internalized via clathrin-mediated endocytosis and is mainly translocated via Rab11a to the ER/ERC for recycling, thus escaping lysosomal degradation. Recycling of $Ca_V1.2$ appears to be the main itinerary during the endocytic trafficking of $Ca_V1.2$.

Translocation of $Ca_V1.2$ to the Rab11a Perinuclear Endocytic Recycling Compartment Depends on an Intact Actin Cytoskeleton but Not on the Microtubule Network

We anticipate that recycling mediated by the actin cytoskeleton is responsible for maintaining stable surface expression of $Ca_V1.2$ during inhibition of microtubule-based transport (Figure 2). To investigate the

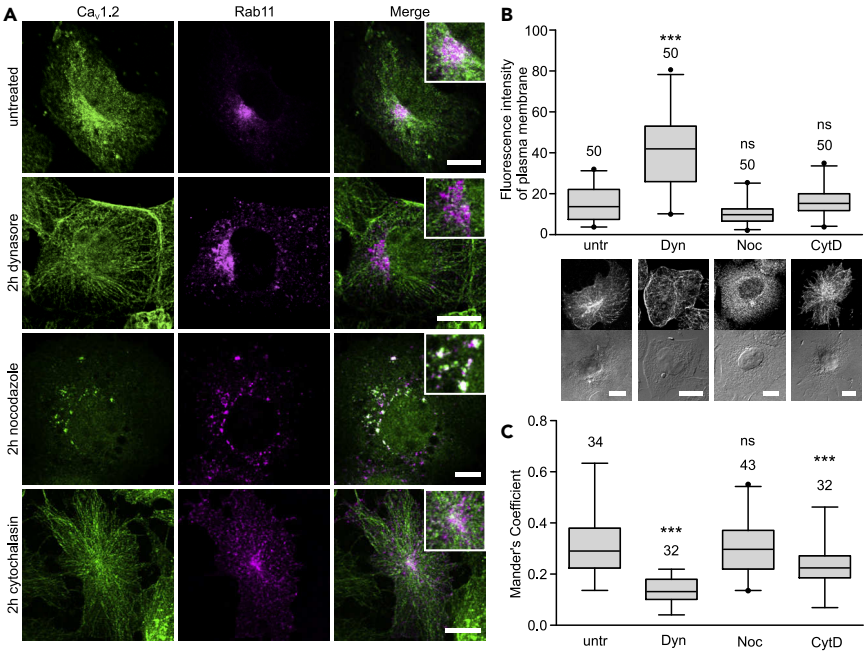

Figure 5. Targeting of Endogenous Ca$_V$1.2 to Rab11a-recycling Compartment in HL-1 Cells Depends on an Intact Actin Cytoskeleton but Not on Microtubules

(A) Laser scanning confocal images of HL-1 expressing Rab11a-mRFP (magenta) and immunostained for Ca$_V$1.2 (green) after 2 hr exposure to the indicated pharmacological agents: dynasore to inhibit clathrin-mediated endocytosis, nocodazole and cytochalasin D to disrupt the microtubule- and actin-based cytoskeleton, respectively. The overlapping pixels appear in white in the merged images shown at the right. Inset shows an enlarged view of the corresponding merged image. Scale bars: 10 μm.

(B) Box plot of the normalized fluorescence intensity at the plasma membrane from cells treated as described in panel (A). For better visualization of the cell membrane, the fluorescence and transmission images of representative cells are shown below. Scale bars: 10 μm. untr, Untreated cells; Dyn, dynasore; Noc, nocodazole; CytD, cytochalasin D. Numbers above each box represent the *n* size. Each box represents the interquartile range (IQR) (25th and 75th quartile) with the median indicated by a line. Whiskers above and below indicate the 95% confidence interval. Outliers are shown by dots. Statistical significance (one-way ANOVA, $p \leq 0.001$).

(C) Box plot of the colocalization analysis between Ca$_V$1.2 and Rab11a, according to Manders' overlap coefficient evaluated after 2 hr of exposure to the indicated drug. Numbers above each box represent the *n* size. Each box represents the IQR (25th and 75th quartile) with the median indicated by a line. Whiskers above and below indicate the 95% confidence interval. Outliers are shown by dots. Statistical significance (one-way ANOVA, $p \leq 0.001$).

dependence of Rab11a-mediated Ca$_V$1.2 recycling on cytoskeletal components, we analyzed the effect of nocodazole and cytochalasin D on the degree of Ca$_V$1.2/Rab11a colocalization (Figure 5). Since during clathrin-mediated endocytosis, dynamin is used for the scission of the endocytic vesicle from the plasma membrane (Maxfield and McGraw, 2004), we used the dynamin-dependent endocytosis inhibitor, dynasore, as control. Inhibition of endocytosis decreases the incoming endosomal traffic, and thus it is expected to increase the cell surface expression of Ca$_V$1.2 and to reduce its entry to the ERC.

HL-1 cells were transfected with a construct encoding a fluorescently labeled Rab11a (Rab11-mRFP), exposed to the corresponding inhibitor for 2 hours, and then immediately fixed and immunostained for Ca$_V$1.2. The suitability of the Rab11-mRFP construct for selectively labeling the ERC was assessed by immunodetection of the fluorescently labeled Rab11a with the anti-Rab11a antibody used in Figure 4. The fluorescence signals overlapped almost completely in the perinuclear region (Figure S4). Cells treated with dynasore show a significant enrichment of the Ca$_V$1.2 fluorescence signal at the plasma membrane and a decreased degree of colocalization between Ca$_V$1.2 and Rab11a, compared with that in non-treated cells (Figure 5). In time-lapse experiments, heterologously expressed HA-tagged Ca$_V$1.2 exhibit longer dwelling times at the plasma membrane of dynasore-treated cells than of untreated cells (Figure S5).

In contrast, exposure of HL-1 cells to nocodazole has no effect on the surface density of the channel, as demonstrated by both electrophysiology (Figure 2) and fluorescence intensity at the cell membrane (Figure 5B), or on its overlap with the Rab11a ERC (Figure 5C). Using double staining for Golgi and Rab11a-ERC, we excluded the possibility that fragmentation of these compartments induced by nocodazole could lead to random overlap between the corresponding scattered fragments (Figure S6).

Depolymerization of actin filaments by cytochalasin D also impaired the delivery of $Ca_V1.2$ into the ERC, as manifested by the decreased MOC value for $Ca_V1.2$ and Rab11a (Figure 5C). However, the surface expression of the channel, as shown electrophysiologically here (Figure 5B) and in a previous report (Stölting et al., 2015), was not altered, in contrast to the results using dynasore.

These results show that Rab11a-mediated translocation of $Ca_V1.2$ to the ERC depends on an intact actin- but not microtubule-based cytoskeleton. They also suggest the existence of diverse cellular strategies for maintaining stable levels of $Ca_V1.2$ at the cell surface by compensating for trafficking dysfunction. However, we found that only impairment of endocytosis results in an excess of channels at the plasma membrane (Figure 5) suggesting that this process is central for the homeostatic regulation of cell surface $Ca_V1.2$.

Disruption of the Actin Cytoskeleton Re-Routes Internalized $Ca_V1.2$ from Recycling to Lysosomal Degradation

To test whether the observed colocalization of $Ca_V1.2$ with Rab11a reflected sorting of newly internalized, rather than *de novo* synthesized, channels into the perinuclear ERC, we monitored the post-endocytic fate of $Ca_V1.2$ in living cells. HL-1 cells cotransfected with $Ca_V1.2$-HA and either fluorescently labeled Rab11a or Lamp1 were subjected to cell surface labeling reaction and imaging using spinning disk microscopy, as described in Figure 3. Time-lapse sequences of the merged images for non-treated cells and cells treated with cytochalasin D are shown in Figure 6. In non-treated HL-1 cells, internalized $Ca_V1.2$ channels are mostly translocated, via Rab11a-positive endosomes, to the ERC where they accumulate over time (Figure 6A, top panel) and delivery of channels to lysosomes (LAMP1) is only marginal (Figure 6A, bottom panel). However, the post-endocytic fate of the channel protein changes dramatically upon disruption of actin filaments with cytochalasin D (Figure 6B). Under such conditions, internalized $Ca_V1.2$ is virtually excluded from the Rab11a-RE/ERC, whereas most of the channels are translocated to lysosomes (Figure 6B).

We estimated the MOC values for $Ca_V1.2$ with either Rab11a or Lamp1 in living cells from the first images of each time-lapse sequence (t = 0). The MOC values show that the degree of overlap changes significantly in the presence of cytochalasin D (Figure 6C). Disruption of the actin cytoskeleton resulted in a decrease of the mean MOC value for $Ca_V1.2$ and Rab11a from 0.52 to 0.32, but produced an increase in overlap between $Ca_V1.2$ and Lamp1 from 0.32 to 0.55.

These results demonstrate that disruption of the actin cytoskeleton re-routes endocytosed $Ca_V1.2$ from recycling to lysosomal degradation. The post-endocytic sorting of $Ca_V1.2$ to the recycling compartment therefore relies on a competent actin cytoskeleton.

DISCUSSION

Normal cardiomyocyte excitability and contractility rely on controlled calcium entry via $Ca_V1.2$ channels. Endocytosis decreases the availability of channels at the plasma membrane, but its contribution to $Ca_V1.2$ regulation is unclear. To maintain steady-state levels of $Ca_V1.2$ at the plasma membrane, the loss of channels due to endocytosis might be compensated by the insertion of new channels from the secretory and/or recycling pathways. Our understanding of $Ca_V1.2$ trafficking pathways in native systems has been limited, partly due to the restricted capability to visualize and dissect channels originating from the different trafficking routes.

Here, using spinning disk microscopy and fluorescence-specific labeling of cell surface $Ca_V1.2$ and the endosomal-lysosomal compartments, we follow the post-endocytic fate of the channel in HL-1 atrial-derived cells. We demonstrated that endocytic recycling mediated by Rab11a is a major trafficking route regulating stable L-type current expression. $Ca_V1.2$ is efficiently internalized via the clathrin-dynamin-mediated pathway and mostly translocated to the recycling compartment via Rab11a, while escaping lysosomal degradation. In ventricular myocardium, Rab11b, another member of the Rab11 family, drives the

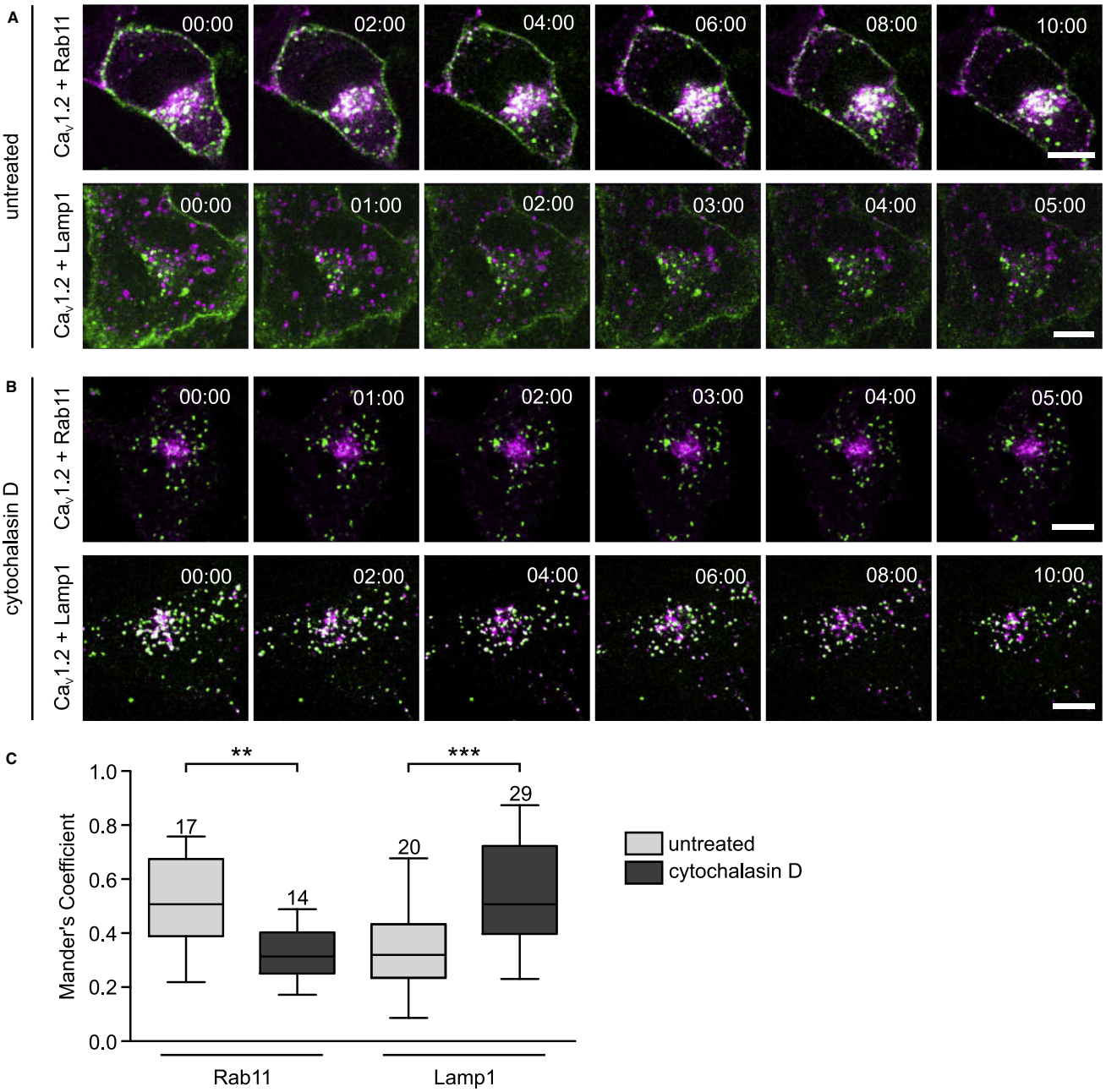

Figure 6. Disruption of the Actin Cytoskeleton Re-routes $Ca_V1.2$ to Lysosomes in HL-1 Cells

(A) Time-lapse sequences of the sorting of internalized $Ca_V1.2$ in HL-1 cells expressing either fluorescently labeled Rab11a or LAMP1 for staining RE/ERC and lysosomes, respectively. $Ca_V1.2$-HA channels at the cell surface were labeled as in Figure 3. The HA-mediated fluorescence signal of the cell surface $Ca_V1.2$ channels is shown in green, and the signal for Rab11a-mRFP and LAMP1-mRFP, in magenta. Only the merged images are shown with the overlapping pixels in white. Scale bar: 10 μm.

(B) Time-lapse sequences of the sorting of internalized $Ca_V1.2$ in HL-1 cells as in *A*, but after pharmacological disruption of the actin cytoskeleton using cytochalasin D. Post-endocytic accumulation of $Ca_V1.2$ in the RE/ERC is severely impaired in the absence of an intact actin cytoskeleton. Scale bar: 10 μm.

(C) Box plot of the colocalization analysis according to Manders' overlap coefficient between $Ca_V1.2$ with either Rab11a or LAMP1 in HL-1 cells in the presence (dark gray boxes) and absence (light gray boxes) of cytochalasin D. MOC was calculated from the images acquired at t = 0. Numbers above each box represent the *n* size. Each box represents the interquartile range (25^{th} and 75^{th} quartile) with the median indicated by a line. Whiskers above and below indicate the 95% confidence interval. Statistical significance (one-way ANOVA, ***$p \leq 0.001$; **$p \leq 0.01$).

degradation of cell surface $Ca_V1.2$ channels (Best et al., 2011). Therefore, either different members of the Rab11 family may differently regulate the endocytic fate of the channel or, alternatively, Rab11-mediated endosomal transport of $Ca_V1.2$ may be tissue-specific.

Perturbation of the microtubule network for at least 20 hr does not alter channel abundance at the surface of HL-1 cells (Figure 2). This suggests that $Ca_V1.2$ can cycle between the plasma membrane and the ERC for at least this period of time without secretory traffic input. In HEK cells the half-life of total cellular $Ca_V1.2$ was calculated to be 3.5 hr (Chien et al., 1995). This rather short half-life possibly reflects the lack of regulatory mechanisms that control channel trafficking, stability, and degradation in heterologous expression systems.

Depolymerization of actin filaments by cytochalasin D impairs the translocation of endocytosed $Ca_V1.2$ to the RE/ERC and diverts the channel to lysosomes (Figure 6), indicating that the entry to the ERC is actin dependent, whereas translocation to lysosomes is not. The internalization of channels in the absence of F-actin suggests that the delivery to the first station along the endocytic pathway, the sorting endosome, is independent of an intact actin cytoskeleton. These results are consistent with the finding that *in vitro* reconstitution of the transferrin receptor transport to recycling endosomes is inhibited by cytochalasin D (Bartz et al., 2003) but its delivery to early/sorting endosomes persists during disruption of the actin cytoskeleton by latrunculin B (Ohashi et al., 2011). We assume that the transport of $Ca_V1.2$ from sorting endosomes to the ERC and from the ERC back to the plasma membrane is mediated by the actin-based motor proteins, myosin V and VI, as reported for other ion channels in cardiac myocytes (Collaco et al., 2010; Lapierre and Goldenring, 2005; Lapierre et al., 2001; Millman et al., 2008; Schumacher-Bass et al., 2014; Swiatecka-Urban et al., 2004, 2007).

We estimated an unprecedented short time constant of internalization of 7.5 ± 0.5 min for $Ca_V1.2$ in HL-1 cells. To our knowledge, this is the first reported τ_{int} for $Ca_V1.2$ in cardiomyocytes. Comparably short times have been obtained only for the $K_V1.5$ voltage-gated potassium channel in HL-1 cells, wherein efficient recycling mediated by Rab11 and Rab4 proved to be relevant for maintaining steady-state levels of the cell surface channels (McEwen et al., 2007). As the cell surface density of $Ca_V1.2$ channels remains unaltered in cells treated with cytochalasin D (Stölting et al., 2015 and Figure 5), we envisage that Rab4-mediated fast recycling maintains channel homeostasis under these conditions. Figure S2 shows that a fraction of newly inserted channels overlaps with preassembled channels stained during the first pulse at the cell periphery. Thus, fast recycling may provide a confined trafficking circuit to regulate local $Ca_V1.2$-mediated signaling.

The question arises why is $Ca_V1.2$ exposed to such a high turnover rate at the cell surface of heart cells? We propose that the dynamic endocytic recycling of $Ca_V1.2$ provides not only a quantitative regulation of the amount of channels at the plasma membrane but also a qualitative control needed to ensure the expression of functional $Ca_V1.2$ channel complexes at the plasma membrane. $Ca_V1.2$ is subjected to extensive regulation by a variety of mechanisms that are vital for cardiac function under normal and stress conditions. These include different types of post-translational modifications and dynamic associations with different modulatory proteins (Oz et al., 2017; Simms et al., 2015). Channel-ligand interactions and post-translational modifications may alter the protein-protein interaction environment of the channel and introduce local unfolding, prompting the channel to undergo quality control.

Among post-translational modifications, phosphorylation of $Ca_V1.2$ via β1-adrenergic receptor activation is a well-established event that facilitates calcium current during the fight-or-flight response (Huang and Zamponi, 2017; Hulme et al., 2006; Oz et al., 2017). Most recently, it has been shown that phosphorylation of $Ca_V1.2$ at one specific site induces a conformational change to the channel and phosphorylation at a further site leads to the displacement of the β-adrenergic receptor (Cserne Szappanos et al., 2017; Patriarchi et al., 2016). Other phosphorylation events also cause alterations to the integrity of the $Ca_V1.2$ macromolecular complex (Altier et al., 2012). Furthermore, phosphorylation of several ion channels, including connexin 43 and $K_V1.3$, induces ubiquitination, followed by internalization and degradation, of these proteins (Martinez-Marmol et al., 2017; Smyth et al., 2014). Ubiquitination and deubiquitination of ion channels, including voltage-gated calcium channels, emerge as regulatory mechanisms controlling their proteosomal degradation after ER exit (Altier et al., 2011; Waithe et al., 2011) and their internalization rate and endosomal sorting (Eaton et al., 2010; Felix and Weiss, 2017; Garcia-Caballero et al., 2014; McCann et al., 2016). The K_{ATP} channel also undergoes rapid internalization and recycling back to the cell surface, and is diverted

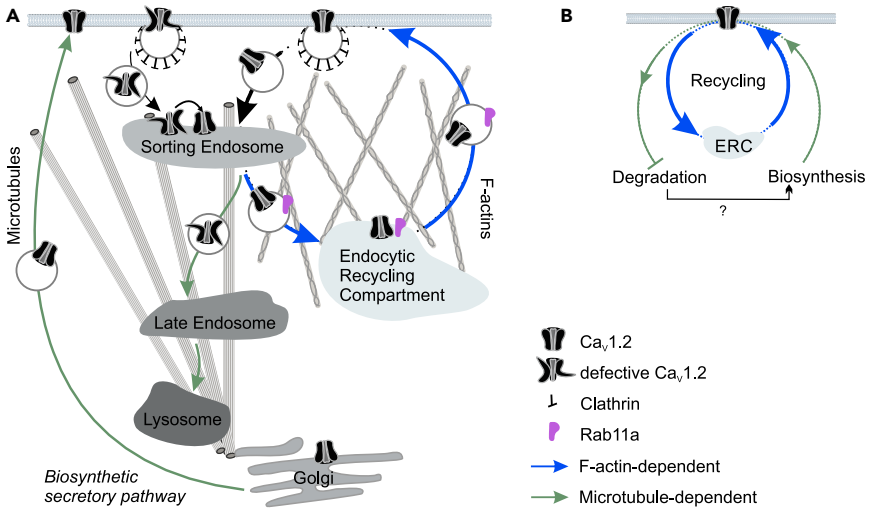

Figure 7. Model for Trafficking Pathway and Regulation of Cell Surface Expression of $Ca_V1.2$ in HL-1 Cells

(A) $Ca_V1.2$ in HL-1 cells is internalized via clathrin-dynamin-dependent endocytosis and mainly recycled back to the plasma membrane via a Rab11a-mediated pathway. The delivery of the channel from sorting endosomes to the endocytic recycling compartment (ERC) and back to the plasma membrane is regulated by actin filaments (blue arrows). Traffic of defective channels from sorting endosomes to lysosomes, as well as of *de novo* channels from the biosynthetic secretory pathway, is mediated by microtubules (green arrows).

(B) The secretory and endosomal transport of $Ca_V1.2$ is depicted as interwoven trafficking pathways. The secretory traffic aids the refilling of the ERC pool upon removal of the channel from the recycling circuit by degradation, via a yet-to-be discovered crosstalk (black arrow).

to lysosomal degradation upon activation of protein kinase C (PKC) (Manna et al., 2010). Conversely, a recent study reported that PKC phosphorylation of $Ca_V1.2$ increases the expression of the channel at the plasma membrane of HL-1 cells (Keren Raifman et al., 2017). As already proposed for Cx43 (Smyth et al., 2014), specific timing and arrangement of phosphorylations of $Ca_V1.2$ might determine the mode of ubiquitination and, in turn, the fate of the internalized protein.

We propose a model in which the post-endocytic trafficking of $Ca_V1.2$ supports the quality control of the channel protein at the sorting endosome (Figure 7A). In this dedicated logistic center, the sorting fate of the $Ca_V1.2$ toward one of two distinct routes, recycling or degradation, is decided according to the channel state and cellular demand. Corrupted channels are translocated to the degradation pathway via microtubule-based transport, whereas the remainder, including post-translationally modified ones, are repaired and, after quality control approval, are recycled back to the plasma membrane via a Rab11a-mediated process along actin filaments. The β-subunit associates directly with F-actin and stimulates the channel surface insertion (Stölting et al., 2015). This subunit may act as a tether to retain internalized channels and confine $Ca_V1.2$-containing endosomes to the cortical actin while preventing the switch to microtubule tracks and diversion to lysosomes. The dynamic interaction of the β-subunit with $Ca_V1.2$ fulfills a critical role in mediating quality control through endocytic recycling; association of the β-subunit with $Ca_V1.2$ ensures normal channel function and survival at the cell surface, whereas its dissociation triggers endocytosis via the dynamin-dependent pathway (Gonzalez-Gutierrez et al., 2007; Hidalgo et al., 2006; Hidalgo and Neely, 2007; Miranda-Laferte et al., 2011). We hypothesize that during internalization $Ca_V1.2$ and $Ca_V\beta$ traffic separately, whereas during forward transport either along the secretory or the recycling pathways, the two subunits associate with each other.

A key remaining question is what is the role of the secretory pathway in $Ca_V1.2$ cell surface homeostasis. After all, a dynamic quality control at the plasma membrane requires active input of *de novo* channels. We found that a large fraction of $Ca_V1.2$, presumably arising from the biosynthetic secretory pathway (Hong et al., 2010), co-distributes lengthwise with tubulin filaments extending from the perinuclear region to the cell periphery (Figure 1). This pool of intracellular channels may provide a reservoir for rapid secretory traffic to respond to physiological demand. We did not observe $Ca_V1.2$ accumulation after disrupting the actin- and microtubule-based transport, suggesting a regulated rather than a constitutive channel

biosynthesis. We envision that the pool of channels residing at the ERC is being constantly monitored and refilled by the secretory pathway through a yet-to-be-established feedback loop that matches degradation and protein translation rates (Figure 7B).

In summary, our findings reveal that the main sorting fate for endocytosed $Ca_V1.2$ is recycling via the Rab11a-mediated pathway. Defects in Rab11-mediated recycling have been associated with several neurological diseases (Li and DiFiglia, 2012), but to date such aberrations have not been directly linked to cardiac disorders. A single point mutation in $Ca_V1.2$ that alters the cell surface density of the channel has been found in a patient with Brugada syndrome (Antzelevitch et al., 2007). It will be interesting to investigate the recycling pathway of $Ca_V1.2$ channels bearing this disease-causing mutation. The present results may help understanding $Ca_V1.2$-trafficking-associated channelopathies and considering new therapeutic perspectives.

Limitations of the Study

Adult cardiomyocytes are not suited for gene transfer of high-molecular-mass cDNA constructs as the one encoding for $Ca_V1.2$ (Christensen et al., 2000, 2003; Gizak et al., 2009; Louch et al., 2011) and they exhibit alterations in protein expression levels, peak L-type Ca^{2+} currents and channel localization, as well as cell morphology during the first 24 hr of culture (Banyasz et al., 2008; Leach et al., 2005; Louch et al., 2004; Mitcheson et al., 1996). This greatly restricts the use of this system for determining the internalization rate and fate of $Ca_V1.2$ and impairs prolonged drug treatment of the cardiomyocytes (Figure 2). In contrast, HL-1 cells retain a rather embryonic phenotype but are well suited for studying trafficking of $Ca_V1.2$.

Although, we cannot prove that our conclusions are valid for adult cardiomyocytes, we believe that the latter is subjected to even a tighter regulatory input to assure proper $Ca_V1.2$-mediated calcium signals. Thus, a comparable dynamic recycling as described for HL-1 cells would be required for maintaining the quality control of the post-translated modified channels. Nevertheless, an additional trafficking route has been described in differentiated mouse cardiomyocytes that delivers $Ca_V1.2$ to the T-tubules along microtubules via BIN1 protein (Hong et al., 2010). Likely, several trafficking routes assuring tight and local control of $Ca_V1.2$ at the plasma membrane coexist in adult cardiomyocytes to support their increased demand for regulatory input.

METHODS

All methods can be found in the accompanying Transparent Methods supplemental file.

SUPPLEMENTAL INFORMATION

Supplemental Information includes Transparent Methods and six figures and can be found with this article online at https://doi.org/10.1016/j.isci.2018.08.012.

ACKNOWLEDGMENTS

We thank Raul Guzman, Ingo Weyand (Forschungszentrum Jülich) for helpful discussions and Arne Franzen (Forschungszentrum Jülich) for generating the $Ca_V1.2$-encoding vector.

AUTHOR CONTRIBUTIONS

R.C. performed, designed, and analyzed all the laser scanning and spinning disk microscopy experiments; prepared the figures; and wrote the manuscript. G.S. performed and analyzed the electrophysiological experiments and prepared the figures. J.H. performed and analyzed the super-resolution experiments, developed the program for data acquisition and analysis, and prepared the corresponding figures. G.R. prepared the samples for super-resolution and performed experiments and analysis. D.K. performed the analysis for the half-time of internalization; T.G. performed super-resolution microscopy analysis. N.J. maintained HL-1 cell culture and performed the transfections. P.H. conceived the project and wrote the manuscript.

DECLARATION OF INTERESTS

The authors declare no competing interests.

Received: May 21, 2018
Revised: July 18, 2018
Accepted: August 10, 2018
Published: September 28, 2018

REFERENCES

Altier, C., Dubel, S.J., Barrere, C., Jarvis, S.E., Stotz, S.C., Scott, J.D., Nargeot, J., Zamponi, G.W., and Bourinet, E. (2012). AKAP79 modulation of L-type channels involves disruption of intramolecular interactions in the $Ca_V1.2$ subunit. Channels (Austin) *6*, 157–165.

Altier, C., Garcia-Caballero, A., Simms, B., You, H., Chen, L., Walcher, J., Tedford, H.W., Hermosilla, T., and Zamponi, G.W. (2011). The $Ca_V\beta$ subunit prevents RFP2-mediated ubiquitination and proteasomal degradation of L-type channels. Nat. Neurosci. *14*, 173–180.

Antzelevitch, C., Pollevick, G.D., Cordeiro, J.M., Casis, O., Sanguinetti, M.C., Aizawa, Y., Guerchicoff, A., Pfeiffer, R., Oliva, A., Wollnik, B., et al. (2007). Loss-of-function mutations in the cardiac calcium channel underlie a new clinical entity characterized by ST-segment elevation, short QT intervals, and sudden cardiac death. Circulation *115*, 442–449.

Banyasz, T., Lozinskiy, I., Payne, C.E., Edelmann, S., Norton, B., Chen, B., Chen-Izu, Y., Izu, L.T., and Balke, C.W. (2008). Transformation of adult rat cardiac myocytes in primary culture. Exp. Physiol. *93*, 370–382.

Bartz, R., Benzing, C., and Ullrich, O. (2003). Reconstitution of vesicular transport to Rab11-positive recycling endosomes in vitro. Biochem. Biophys. Res. Commun. *312*, 663–669.

Basheer, W.A., and Shaw, R.M. (2016). Connexin 43 and $Ca_V1.2$ ion channel trafficking in healthy and diseased myocardium. Circ. Arrhythm. Electrophysiol. *9*, e001357.

Best, J.M., Foell, J.D., Buss, C.R., Delisle, B.P., Balijepalli, R.C., January, C.T., and Kamp, T.J. (2011). Small GTPase Rab11b regulates degradation of surface membrane L-type $Ca_V1.2$ channels. American journal of physiology. Cell Physiol. *300*, C1023–C1033.

Bodi, I., Mikala, G., Koch, S.E., Akhter, S.A., and Schwartz, A. (2005). The L-type calcium channel in the heart: the beat goes on. J. Clin. Invest. *115*, 3306–3317.

Bolte, S., and Cordelieres, F.P. (2006). A guided tour into subcellular colocalization analysis in light microscopy. J. Microsc. *224*, 213–232.

Catalucci, D., Zhang, D.H., DeSantiago, J., Aimond, F., Barbara, G., Chemin, J., Bonci, D., Picht, E., Rusconi, F., Dalton, N.D., et al. (2009). Akt regulates L-type Ca^{2+} channel activity by modulating $Ca_V\alpha_1$ protein stability. J. Cell Biol. *184*, 923–933.

Chien, A.J., Zhao, X.L., Shirokov, R.E., Puri, T.S., Chang, C.F., Sun, D., Rios, E., and Hosey, M.M. (1995). Roles of a membrane-localized β-subunit in the formation and targeting of functional L-type Ca^{2+} channels. J. Biol. Chem. *270*, 30036–30044.

Christensen, G., Gruber, P.J., Wang, Y., and Chien, K.R. (2003). Embryonic and neonatal cardiac gene transfer in vivo. Methods Mol. Biol. *219*, 169–178.

Christensen, G., Minamisawa, S., Gruber, P.J., Wang, Y., and Chien, K.R. (2000). High-efficiency, long-term cardiac expression of foreign genes in living mouse embryos and neonates. Circulation *101*, 178–184.

Cole, N.B., Sciaky, N., Marotta, A., Song, J., and Lippincott-Schwartz, J. (1996). Golgi dispersal during microtubule disruption: regeneration of Golgi stacks at peripheral endoplasmic reticulum exit sites. Mol. Biol. Cell *7*, 631–650.

Collaco, A., Jakab, R., Hegan, P., Mooseker, M., and Ameen, N. (2010). a-AP-2 directs Myosin VI-dependent endocytosis of cystic fibrosis transmembrane conductance regulator chloride channels in the intestine. J. Biol. Chem. *285*, 17177–17187.

Cserne Szappanos, H., Muralidharan, P., Ingley, E., Petereit, J., Millar, H.A., and Hool, L.C. (2017). Identification of a novel cAMP dependent protein kinase A phosphorylation site on the human cardiac calcium channel. Sci. Rep. *7*, 15118.

Dick, I.E., Joshi-Mukherjee, R., Yang, W., and Yue, D.T. (2016). Arrhythmogenesis in Timothy Syndrome is associated with defects in Ca^{2+}-dependent inactivation. Nat. Commun. *7*, 10370.

Eaton, D.C., Malik, B., Bao, H.F., Yu, L., and Jain, L. (2010). Regulation of epithelial sodium channel trafficking by ubiquitination. Proc. Am. Thorac. Soc. *7*, 54–64.

Efron, B., and Tibshirani, R.J. (1993). An Introduction to the Bootstrap. Monographs on Statistics and Applied Probability (Chapman & Hall/CRC).

Felix, R., and Weiss, N. (2017). Ubiquitination and proteasome-mediated degradation of voltage-gated Ca^{2+} channels and potential pathophysiological implications. Gen. Physiol. Biophys. *36*, 1–5.

Garcia-Caballero, A., Gadotti, V.M., Stemkowski, P., Weiss, N., Souza, I.A., Hodgkinson, V., Bladen, C., Chen, L., Hamid, J., Pizzoccaro, A., et al. (2014). The deubiquitinating enzyme USP5 modulates neuropathic and inflammatory pain by enhancing $Ca_V3.2$ channel activity. Neuron *83*, 1144–1158.

Gizak, A., Maciaszczyk-Dziubinska, E., Jurowicz, M., and Rakus, D. (2009). Muscle FBPase is targeted to nucleus by its 203KKKGK207 sequence. Proteins *77*, 262–267.

Gonzalez-Gutierrez, G., Miranda-Laferte, E., Neely, A., and Hidalgo, P. (2007). The Src Homology 3 Domain of the β-subunit of voltage-gated calcium channels promotes endocytosis via Dynamin interaction. J. Biol. Chem. *282*, 2156–2162.

Green, E.M., Barrett, C.F., Bultynck, G., Shamah, S.M., and Dolmetsch, R.E. (2007). The tumor suppressor eIF3e mediates calcium-dependent internalization of the L-type calcium channel $Ca_V1.2$. Neuron *55*, 615–632.

Hao, M., and Maxfield, F.R. (2000). Characterization of rapid membrane internalization and recycling. J. Biol. Chem. *275*, 15279–15286.

Hidalgo, P., Gonzalez-Gutierrez, G., Garcia-Olivares, J., and Neely, A. (2006). The α_1-β-subunit interaction that modulates calcium channel activity is reversible and requires a competent a-interaction domain. J. Biol. Chem. *281*, 24104–24110.

Hidalgo, P., and Neely, A. (2007). Multiplicity of protein interactions and functions of the voltage-gated calcium channel β-subunit. Cell Calcium *42*, 389–396.

Hofmann, F., Flockerzi, V., Kahl, S., and Wegener, J.W. (2014). L-type $Ca_V1.2$ calcium channels: from in vitro findings to in vivo function. Physiol. Rev. *94*, 303–326.

Hong, T.T., Smyth, J.W., Chu, K.Y., Vogan, J.M., Fong, T.S., Jensen, B.C., Fang, K., Halushka, M.K., Russell, S.D., Colecraft, H., et al. (2012). BIN1 is reduced and CaV1.2 trafficking is impaired in human failing cardiomyocytes. Heart Rhythm *9*, 812–820.

Hong, T.T., Smyth, J.W., Gao, D., Chu, K.Y., Vogan, J.M., Fong, T.S., Jensen, B.C., Colecraft, H.M., and Shaw, R.M. (2010). BIN1 localizes the L-type calcium channel to cardiac T-tubules. PLoS Biol. *8*, e1000312.

Huang, J., and Zamponi, G.W. (2017). Regulation of voltage gated calcium channels by GPCRs and post-translational modification. Curr. Opin. Pharmacol. *32*, 1–8.

Hulme, J.T., Westenbroek, R.E., Scheuer, T., and Catterall, W.A. (2006). Phosphorylation of serine 1928 in the distal C-terminal domain of cardiac $Ca_V1.2$ channels during β1-adrenergic regulation. Proc. Natl. Acad. Sci. USA *103*, 16574–16579.

Keren Raifman, T., Kumar, P., Haase, H., Klussmann, E., Dascal, N., and Weiss, S. (2017). Protein kinase C enhances plasma membrane expression of cardiac L-type calcium channel, $Ca_V1.2$. Channels (Austin) *11*, 1–12.

Lapierre, L.A., and Goldenring, J.R. (2005). Interactions of Myosin Vb with Rab11 family members and cargoes traversing the plasma membrane recycling system. Methods Enzymol. *403*, 715–723.

Lapierre, L.A., Kumar, R., Hales, C.M., Navarre, J., Bhartur, S.G., Burnette, J.O., Provance, D.W., Jr.,

Mercer, J.A., Bahler, M., and Goldenring, J.R. (2001). Myosin Vb is associated with plasma membrane recycling systems. Mol. Biol. Cell *12*, 1843–1857.

Larsen, J.K., Mitchell, J.W., and Best, P.M. (2002). Quantitative analysis of the expression and distribution of calcium channel α_1 subunit mRNA in the atria and ventricles of the rat heart. J. Mol. Cell Cardiol. *34*, 519–532.

Leach, R.N., Desai, J.C., and Orchard, C.H. (2005). Effect of cytoskeleton disruptors on L-type Ca channel distribution in rat ventricular myocytes. Cell Calcium *38*, 515–526.

Li, X., and DiFiglia, M. (2012). The recycling endosome and its role in neurological disorders. Prog. Neurobiol. *97*, 127–141.

Link, S., Meissner, M., Held, B., Beck, A., Weissgerber, P., Freichel, M., and Flockerzi, V. (2009). Diversity and developmental expression of L-type calcium channel β2 proteins and their influence on calcium current in murine heart. J. Biol. Chem. *284*, 30129–30137.

Louch, W.E., Bito, V., Heinzel, F.R., Macianskiene, R., Vanhaecke, J., Flameng, W., Mubagwa, K., and Sipido, K.R. (2004). Reduced synchrony of Ca^{2+} release with loss of T-tubules- a comparison to Ca^{2+} release in human failing cardiomyocytes. Cardiovasc. Res. *62*, 63–73.

Louch, W.E., Sheehan, K.A., and Wolska, B.M. (2011). Methods in cardiomyocyte isolation, culture, and gene transfer. J. Mol. Cell. Cardiol. *51*, 288–298.

Manna, P.T., Smith, A.J., Taneja, T.K., Howell, G.J., Lippiat, J.D., and Sivaprasadarao, A. (2010). Constitutive endocytic recycling and protein kinase C-mediated lysosomal degradation control $K_{(ATP)}$ channel surface density. J. Biol. Chem. *285*, 5963–5973.

Martinez-Marmol, R., Styrczewska, K., Perez-Verdaguer, M., Vallejo-Gracia, A., Comes, N., Sorkin, A., and Felipe, A. (2017). Ubiquitination mediates $K_V1.3$ endocytosis as a mechanism for protein kinase C-dependent modulation. Sci. Rep. *7*, 42395.

Maxfield, F.R., and McGraw, T.E. (2004). Endocytic recycling. Nat. Rev. Mol. Cell Biol. *5*, 121–132.

McCann, A.P., Scott, C.J., Van Schaeybroeck, S., and Burrows, J.F. (2016). Deubiquitylating enzymes in receptor endocytosis and trafficking. Biochem. J. *473*, 4507–4525.

McEwen, D.P., Schumacher, S.M., Li, Q., Benson, M.D., Iniguez-Lluhi, J.A., Van Genderen, K.M., and Martens, J.R. (2007). Rab-GTPase-dependent endocytic recycling of $K_v1.5$ in atrial myocytes. J. Biol. Chem. *282*, 29612–29620.

McMahon, H.T., and Boucrot, E. (2011). Molecular mechanism and physiological functions of clathrin-mediated endocytosis. Nat. Rev. Mol. Cell Biol. *12*, 517–533.

Millman, E.E., Zhang, H., Zhang, H., Godines, V., Bean, A.J., Knoll, B.J., and Moore, R.H. (2008). Rapid recycling of β-adrenergic receptors is dependent on the actin cytoskeleton and Myosin Vb. Traffic *9*, 1958–1971.

Miranda-Laferte, E., Gonzalez-Gutierrez, G., Schmidt, S., Zeug, A., Ponimaskin, E.G., Neely, A., and Hidalgo, P. (2011). Homodimerization of the Src homology 3 domain of the calcium channel β-subunit drives dynamin-dependent endocytosis. J. Biol. Chem. *286*, 22203–22210.

Mitcheson, J.S., Hancox, J.C., and Levi, A.J. (1996). Action potentials, ion channel currents and transverse tubule density in adult rabbit ventricular myocytes maintained for 6 days in cell culture. Pflugers Arch. *431*, 814–827.

Ohashi, E., Tanabe, K., Henmi, Y., Mesaki, K., Kobayashi, Y., and Takei, K. (2011). Receptor sorting within endosomal trafficking pathway is facilitated by dynamic actin filaments. PLoS One *6*, e19942.

Oz, S., Pankonien, I., Belkacemi, A., Flockerzi, V., Klussmann, E., Haase, H., and Dascal, N. (2017). Protein kinase A regulates C-terminally truncated $Ca_V1.2$ in *Xenopus* oocytes: roles of N- and C-termini of the α_{1C} subunit. J. Physiol. *595*, 3181–3202.

Patriarchi, T., Qian, H., Di Biase, V., Malik, Z.A., Chowdhury, D., Price, J.L., Hammes, E.A., Buonarati, O.R., Westenbroek, R.E., Catterall, W.A., et al. (2016). Phosphorylation of $Ca_V1.2$ on S1928 uncouples the L-type Ca^{2+} channel from the β2 adrenergic receptor. EMBO J. *35*, 1330–1345.

Rusconi, F., Ceriotti, P., Miragoli, M., Carullo, P., Salvarani, N., Rocchetti, M., Di Pasquale, E., Rossi, S., Tessari, M., Caprari, S., et al. (2016). Peptidomimetic targeting of $Ca_V\beta_2$ overcomes dysregulation of the L-Type calcium channel density and recovers cardiac function. Circulation *134*, 534–546.

Schotten, U., Haase, H., Frechen, D., Greiser, M., Stellbrink, C., Vazquez-Jimenez, J.F., Morano, I., Allessie, M.A., and Hanrath, P. (2003). The L-type Ca^{2+}-channel subunits α_{1C} and β_2 are not downregulated in atrial myocardium of patients with chronic atrial fibrillation. J. Mol. Cell. Cardiol. *35*, 437–443.

Schuh, M. (2011). An actin-dependent mechanism for long-range vesicle transport. Nat. Cell Biol. *13*, 1431–1436.

Schumacher-Bass, S.M., Vesely, E.D., Zhang, L., Ryland, K.E., McEwen, D.P., Chan, P.J., Frasier, C.R., McIntyre, J.C., Shaw, R.M., and Martens, J.R. (2014). Role for Myosin V motor proteins in the selective delivery of K_v channel isoforms to the membrane surface of cardiac myocytes. Circ. Res. *114*, 982–992.

Seisenberger, C., Specht, V., Welling, A., Platzer, J., Pfeifer, A., Kuhbandner, S., Striessnig, J., Klugbauer, N., Feil, R., and Hofmann, F. (2000). Functional embryonic cardiomyocytes after disruption of the L-type α_{1C} ($Ca_V1.2$) calcium channel gene in the mouse. J. Biol. Chem. *275*, 39193–39199.

Shaw, R.M., and Colecraft, H.M. (2013). L-type calcium channel targeting and local signalling in cardiac myocytes. Cardiovasc. Res. *98*, 177–186.

Simms, B.A., Souza, I.A., Rehak, R., and Zamponi, G.W. (2015). The $Ca_V1.2$ N terminus contains a CaM kinase site that modulates channel trafficking and function. Pflugers Arch. *467*, 677–686.

Simms, B.A., and Zamponi, G.W. (2012). The Brugada syndrome mutation A39V does not affect surface expression of neuronal rat $Ca_V1.2$ channels. Mol. Brain *5*, 9.

Smyth, J.W., Zhang, S.S., Sanchez, J.M., Lamouille, S., Vogan, J.M., Hesketh, G.G., Hong, T., Tomaselli, G.F., and Shaw, R.M. (2014). A 14-3-3 mode-1 binding motif initiates gap junction internalization during acute cardiac ischemia. Traffic *15*, 684–699.

Splawski, I., Timothy, K.W., Decher, N., Kumar, P., Sachse, F.B., Beggs, A.H., Sanguinetti, M.C., and Keating, M.T. (2005). Severe arrhythmia disorder caused by cardiac L-type calcium channel mutations. Proc. Natl. Acad. Sci. USA *102*, 8086–8088, discussion.

Splawski, I., Timothy, K.W., Sharpe, L.M., Decher, N., Kumar, P., Bloise, R., Napolitano, C., Schwartz, P.J., Joseph, R.M., Condouris, K., et al. (2004). $Ca_V1.2$ calcium channel dysfunction causes a multisystem disorder including arrhythmia and autism. Cell *119*, 19–31.

Stölting, G., de Oliveira, R.C., Guzman, R.E., Miranda-Laferte, E., Conrad, R., Jordan, N., Schmidt, S., Hendriks, J., Gensch, T., and Hidalgo, P. (2015). Direct interaction of $Ca_V\beta$ with actin up-regulates L-type calcium currents in HL-1 cardiomyocytes. J. Biol. Chem. *290*, 4561–4572.

Swiatecka-Urban, A., Boyd, C., Coutermarsh, B., Karlson, K.H., Barnaby, R., Aschenbrenner, L., Langford, G.M., Hasson, T., and Stanton, B.A. (2004). Myosin VI regulates endocytosis of the cystic fibrosis transmembrane conductance regulator. J. Biol. Chem. *279*, 38025–38031.

Swiatecka-Urban, A., Talebian, L., Kanno, E., Moreau-Marquis, S., Coutermarsh, B., Hansen, K., Karlson, K.H., Barnaby, R., Cheney, R.E., Langford, G.M., et al. (2007). Myosin Vb is required for trafficking of the cystic fibrosis transmembrane conductance regulator in Rab11a-specific apical recycling endosomes in polarized human airway epithelial cells. J. Biol. Chem. *282*, 23725–23736.

Tang, Y., Dai, L., Zhang, X., Li, J., Hendriks, J., Fan, X., Gruteser, N., Meisenberg, A., Baumann, A., Katranidis, A., and Gensch, T. (2015). SNSMIL, a real-time single molecule identification and localization algorithm for super-resolution fluorescence microscopy. Sci. Rep. *5*, 11073.

Waithe, D., Ferron, L., Page, K.M., Chaggar, K., and Dolphin, A.C. (2011). β-subunits promote the expression of $Ca_V2.2$ channels by reducing their proteasomal degradation. J. Biol. Chem. *286*, 9598–9611.

Weissgerber, P., Held, B., Bloch, W., Kaestner, L., Chien, K.R., Fleischmann, B.K., Lipp, P., Flockerzi, V., and Freichel, M. (2006). Reduced cardiac L-type Ca^{2+} current in $Ca_V\beta_2^{-/-}$ embryos impairs cardiac development and contraction with secondary defects in vascular maturation. Circ.Res. *99*, 749–757.

Xiao, S., and Shaw, R.M. (2015). Cardiomyocyte protein trafficking: relevance to heart disease and opportunities for therapeutic intervention. Trends Cardiovasc. Med. *25*, 379–389.

ISCI, Volume 7

Supplemental Information

Rapid Turnover of the Cardiac L-Type $Ca_V1.2$ Channel by Endocytic Recycling Regulates Its Cell Surface Availability

Rachel Conrad, Gabriel Stölting, Johnny Hendriks, Giovanna Ruello, Daniel Kortzak, Nadine Jordan, Thomas Gensch, and Patricia Hidalgo

Supplemental Figures

Figure S1

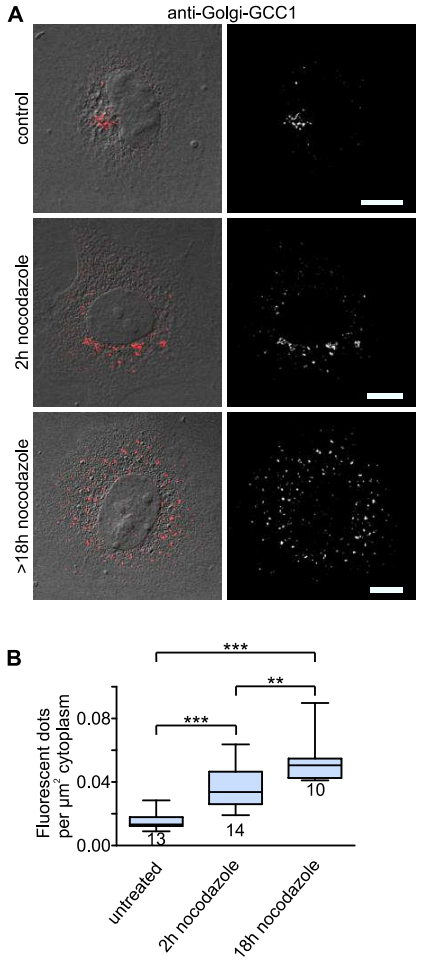

Figure S1. Prolonged nocodazole treatment induces Golgi scattering without changes in the peak amplitude of L-type currents, Related to Figure 2.

(A) Laser scanning confocal images of HL-1 cells stained with anti-Golgi-GCC1 antibody in untreated (control) cells and after incubation with nocodazole for either 2 h or 18 h. For clarity, the fluorescent (shown in red) and transmission images were superimposed and shown in the left panels. The fluorescence images alone are also shown in white and black (right panels) for better visualization of the signal analyzed. Scale bars: 10 µm.

(B) Box plot of the number of fluorescent dots per area for control HL-1 cells and HL-1 cells either exposed to 2 or 18 h to nocodazole as shown in *A*. Numbers below each box represent the number of cells analyzed. Each box represents the IQR (25^{th} and 75^{th} quartile) with the median indicated by a line. Whiskers above and below indicate the 95% confidence interval. Statistical significance (One-Way ANOVA, ***$p \leq 0.001$; ** $p \leq 0.01$). Despite the changes in Golgi fragmentation induced by nocodazole, HL-1 cells treated with the same nocodazole regime showed no alterations of the L-type current density amplitudes and voltage dependence of activation compared to control cells (Main text Figure 2).

Figure S2

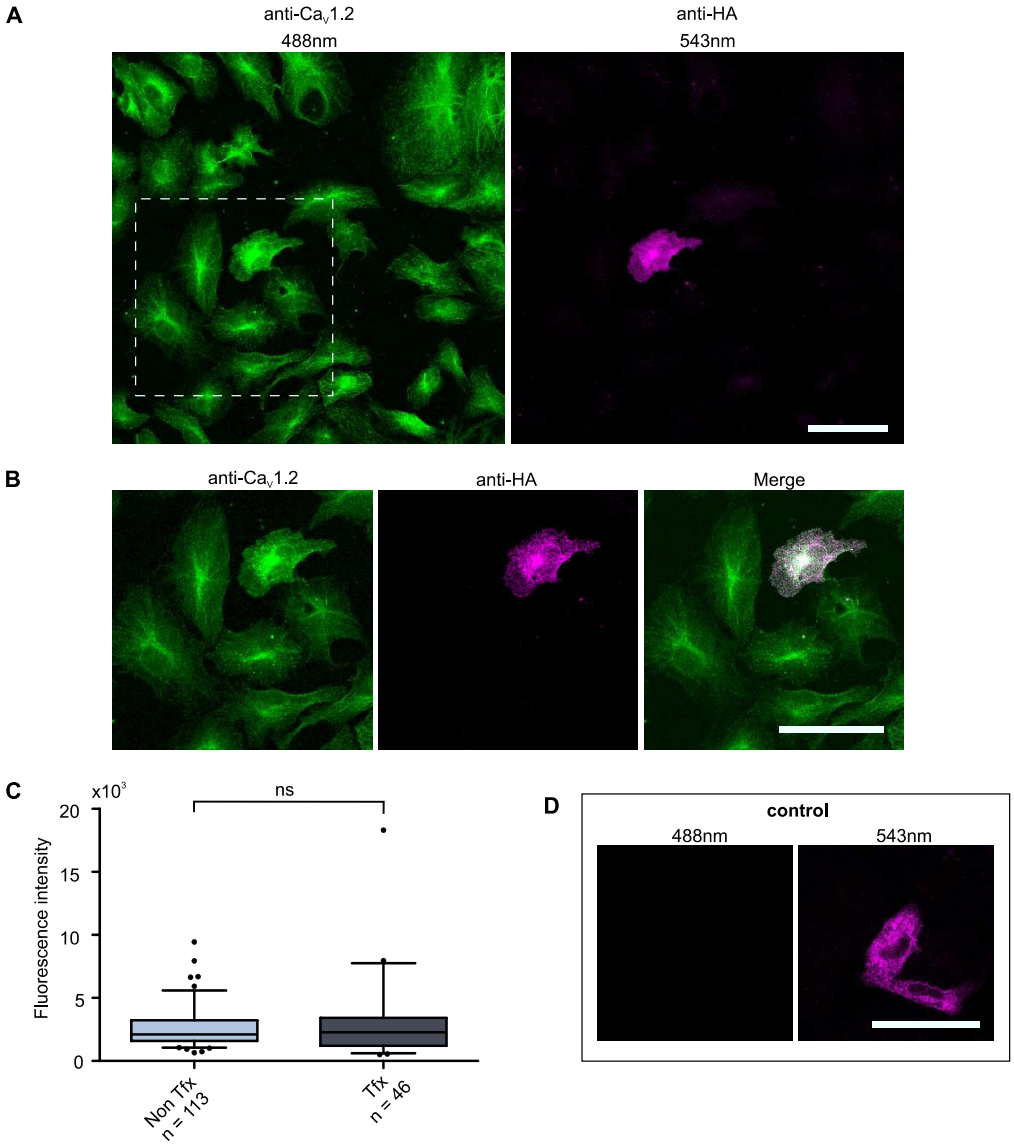

Figure S2. Comparable expression levels of $Ca_V1.2$ in transfected and untransfected HL-1 cells, Related to Figure 3.

(A) Laser scanning confocal images of HL-1 cells transfected with $Ca_V1.2$-HA- and $Ca_V\beta$-subunit-encoding plasmids and immunostained for $Ca_V1.2$ (green) and HA (magenta).

(B) Enlarged view of the marked square region including a representative transfected cell.

(C) Box plot of the fluorescence intensity from anti-CaV1.2 labeled channels measured in entire cells either expressing CaV1.2-HA (Tfx n = 46) or non-expressing (non Tfx n = 113).

(D) Control laser scanning confocal images of HL-1 cells transfected with $Ca_V1.2$-HA- and $Ca_V\beta$-subunit-encoding plasmids and immunostained for only HA-Tag (magenta). No fluorescence of the HA-Tag is visible by exciting with the 488 nm laser.

Significance tested with t-test with Welch‘s correction, p = 0.05. Scale bars: 50µm.

Figure S3

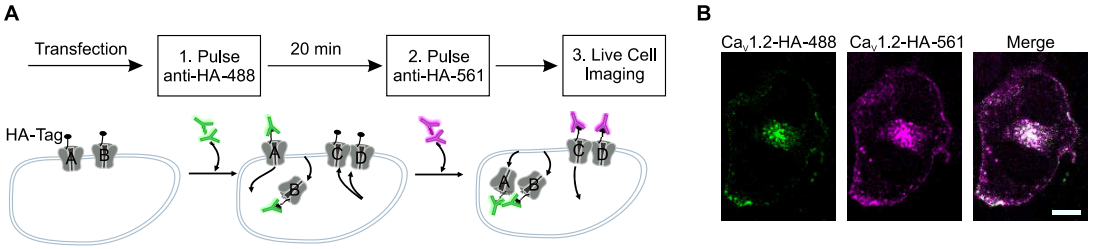

Figure S3. Fluorescence images of HL-1 cells expressing extracellularly HA-tagged Ca$_V$1.2 exposed to a dual-pulse labeling protocol demonstrate channel turnover within a few tens of minutes, Related to Figure 3.

(A) Dual-pulse labelling protocol combined with spinning disk confocal microscopy was used to visualize newly-inserted Ca$_V$1.2 channels in HL-1 cells. HL-1 cells were transfected with a cDNA encoding for Ca$_V$1.2-HA channels and for Ca$_V$β. Two consecutive labelling reactions, with anti-HA-DyLight 488 (step1, shown in green) and DyLight 561 (step2, shown in magenta), were performed 20 min apart and cells were immediately imaged after the second pulse (step 3). The scheme shows channels stained during the first antibody pulse (Ca$_V$1.2-HA-488), denoted with A and B, and during the second antibody pulse (Ca$_V$1.2-HA-561), denoted with C and D. Only Ca$_V$1.2 channels inserted after the first pulse (C and D) can be stained during the second pulse and represent the newly-inserted channel pool.

(B) Representative HL-1 cell showing Ca$_V$1.2 channels stained during anti-HA-488 and anti-HA-561 antibody pulses in green and in magenta, respectively. The merge image is shown in the right panel with overlapping pixels in white. Scale bar: 10 µm.

Figure S4

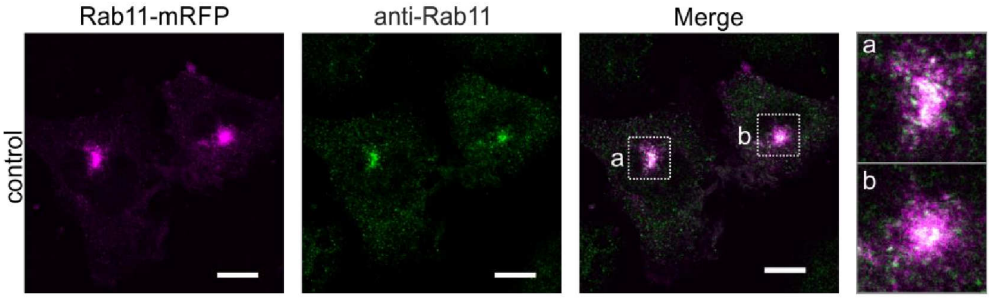

Figure S4. Immunodetected Rab11a colocalizes with heterologously expressed Rab11a-mRFP in HL-1 cells, Related to Figure 5.

Laser scanning confocal images of HL-1 cells expressing Rab11a-mRFP (magenta) and immunostained with anti-Rab11a antibody (green). Overlapping pixels appear in white in the merged figure. Panels at the right show an enlarged view of the corresponding marked square regions from the merged image. Scale bar: 10 µm.

Figure S5

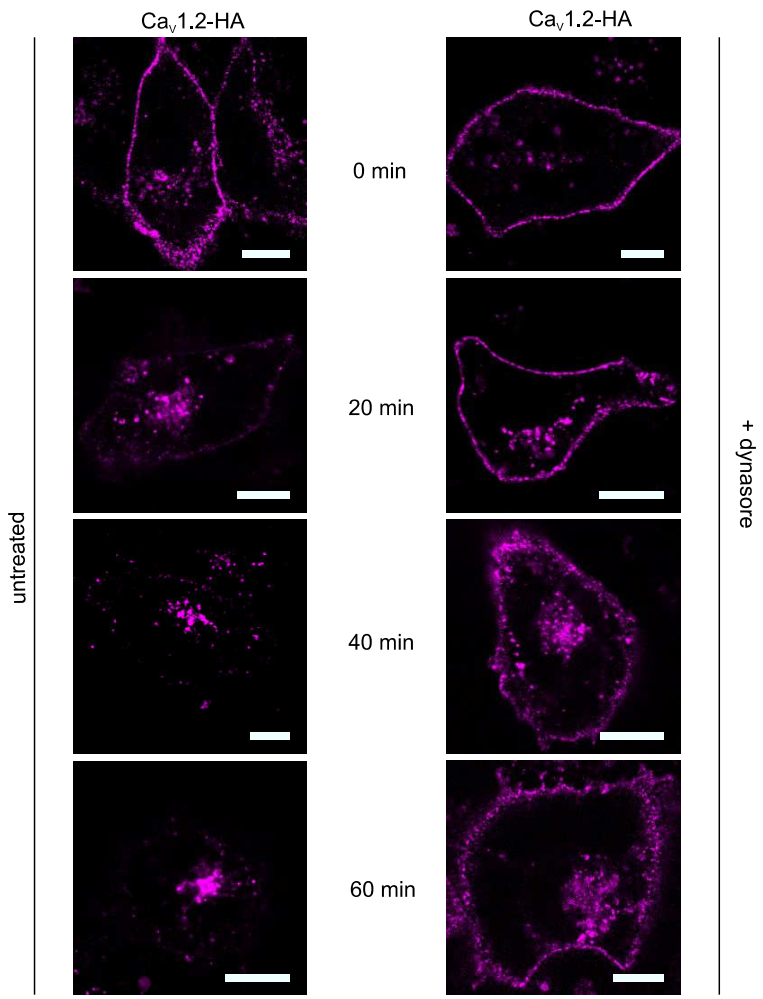

Figure S5. Ca$_V$1.2-HA channels exhibit longer dwelling times at the plasma membrane of dynasore-treated HL-1 cells than of untreated cells, Related to Figure 5.

Laser scanning confocal images of HL-1 cells expressing HA-tagged Ca$_V$1.2 and Ca$_V$β. Cells were stained with anti-HA-DyLight 561 and visualized at different time points after the staining procedure (0, 20, 40, 60 min). Cells were either untreated (left images) or treated with 80 µM dynasore one hour before and during the staining process (right images). Dynasore-treated cells show a prominent membrane staining up to 60 min, while in untreated cells the membrane staining disappeared after 20 min. Scale bar: 10µm

Figure S6

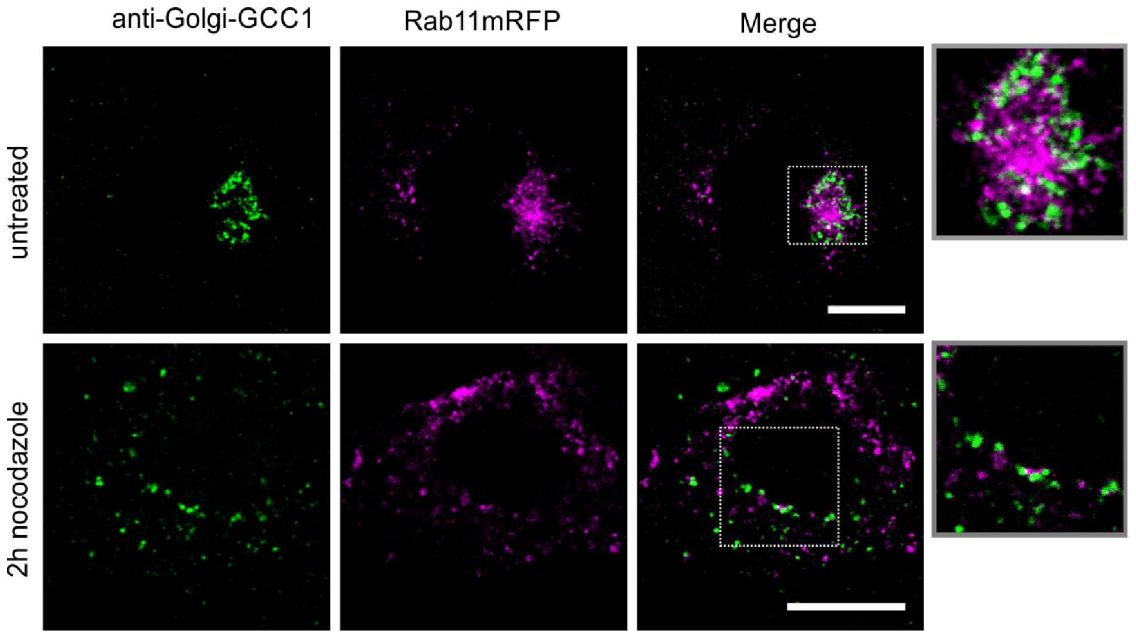

Figure S6. Nocodazole treatment does not result in random overlapping of dispersed fragments from Golgi and Rab11a-endocytic recycling compartment, Related to Figure 5.

Laser scanning confocal images of HL-1 cells expressing Rab11a-mRFP (magenta) and stained with anti-Golgi-GCC1 antibody (green) in untreated cells and after exposing the cells for 2 h to nocodazole. Overlapping pixels appear in white in the merge figures. Right panels correspond to the enlargement of the corresponding marked squares in the merged images. Scale bars: 10 µm.

Transparent Methods

cDNA constructs. The plasmid encoding $Ca_V1.2$-HA was generated by inserting the HA-Tag into the external II-III loop of the rabbit $Ca_V1.2$ pore-forming alpha subunit (accession number UniProtKB P15381) into the pcDNA3.1(+) vector. The coding region of the rat β-subunit (accession number UniProtKB Q8VGC3-2) was subcloned in pcDNA3.1(+) vector by standard techniques. The plasmid encoding the rat lysosomal membrane glycoprotein 1 (Lamp1) fused to the monomeric red fluorescent protein (mRFP) (Lamp1-mRFP) was a gift from Walther Mothes (Addgene plasmid # 1817). The coding regions of Rab7 (Addgene plasmid # 61803) and Rab11 (a gift from Richard Pagano (Addgene plasmid # 12605) were subcloned by standard techniques into mRFP vector (pmRFP) to express Rab proteins coupled to mRFP as described (Guzman et al., 2015).

Cell culture and transfection. The murine atrial cardiomyocyte cell line HL-1 (a kind gift from Dr. W.C. Claycomb) was grown in Claycomb media supplemented with 10% fetal bovine serum (SigmaAldrich), 10 µM norepinephrine (SigmaAldrich), 2 mM L-glutamine (SigmaAldrich) and 100 U/ml penicillin/streptomycin (ThermoFisher Scientific) at 37°C in 5% CO_2 as described (Stölting et al. 2015). Exchange of media was done every 24–48 h. HL-1 cells were seeded 1–2 days prior to performing the corresponding experiment on fibronectin precoated 18 mm glass coverslips for laser scanning confocal microscopy on immunostained fixed cells, 35 mm dishes (ibidi) for live cell imaging using spinning disk microscopy, 8-well plates (ibidi) for single molecule localization microscopy and on 25 mm glass coverslips for electrophysiology.
Cells were transfected with $Ca_V1.2$- and $Ca_V\beta_{2a}$-encoding plasmids (2:1) (Figure 3) and the same mixture with or without Rab11a- or Lamp1-encoding plasmids (Figure 6) using Lipofectamine 2000 (ThermoFisher Scientific). Live cell imaging was performed 24 h after transfection in phenol-red-free DMEM media (ThermoFischer Scientific).

Pharmacological treatment. To disrupt actin filaments, HL-1 cells were incubated for 2 h in medium (DMEM) containing 10 µM cytochalasin D (SigmaAldrich) at 37°C in 5% CO_2. Afterwards the medium was replaced and cells were washed with PBS and fixed with 4% paraformaldehyde (SigmaAldrich). For the disruption of microtubules, HL-1 cells were incubated for the indicated time periods in medium (DMEM) containing 33 µM nocodazole (SigmaAldrich) at 37°C in 5% CO_2 and fixed as described above. To inhibit endocytosis, cells were treated for 2 h with 80 µM dynasore (SigmaAldrich) before fixation.

Cell fixation and immunostaining. The following antibodies were used at the indicated dilutions: rabbit anti-$Ca_V1.2$-ATTO-488 (1:200, Alomone labs), mouse anti-β-tubulin (1:500,

ThermoFisher Scientific), mouse anti-Clathrin (1:100; BD Bioscience), mouse anti-Rab11-D3 (1:250, Santa Cruz), mouse anti-Rab7-B3 (1:250; Santa Cruz) and rabbit anti-Golgi-GCC1 (1:500, BD Bioscience). The fluorophore-conjugated secondary antibodies donkey anti-mouse antibody coupled to Cy3 or Cy5 (1:200, Dianova) or donkey anti-rabbit-Cy3 (1:200, Dianova) was used. Actin filaments were stained with phalloidin coupled to Alexa Fluor 647 (1:500; Invitrogen). HL-1 cells were fixed with 4% paraformaldehyde (PFA; SigmaAldrich) in PBS onto a 37°C heat plate for 5 minutes. All following steps were done at room temperature. Fixed cells were simultaneously permeabilized, blocked and incubated with the corresponding primary antibody using 5% chemiBLOCKER (Merck) supplemented with 0.05% Triton-X100 for 1 h. Cells were then washed twice with PBS and stained with the appropriate secondary antibody for 30 minutes in 5% chemiBLOCKER-0.05% Triton. After washing the cells (twice with PBS) coverslips were mounted on glass slides using Aqua Poly Mount (Polysciences) and stored at 4°C until use.

Immunofluorescent staining of living cells. Transiently transfected HL-1 cells with $Ca_V1.2$-HA were washed with ice cold PBS and stained with mouse anti-HA Tag DyLight 561 or DyLight 488 (1:100, ThermoFisher) in media (OptiMEM) for 10 minutes at room temperature. Immediately after washing, the cells were mounted on the microscope Stage Top Chamber (Okolab) incubator at 37°C for live cell imaging using spinning disk confocal microscopy.
For the pulse chase experiment, HL-1 cells were first stained with the mouse anti-HA Tag DyLight 488 as above, incubated for 20 minutes at 37°C and 5% CO_2 and stained again using mouse anti-HA Tag DyLight 561. Following the washing step, cells were immediately mounted in the spinning disk confocal microscope for live cell imaging.

Laser scanning confocal fluorescence microscopy. Confocal imaging was carried out on a Leica inverted confocal microscope using a 63x/1.4 NA oil immersion objective (Nikon). To visualize Atto488 fluorescence, cells were excited with a 488nm argon laser. For Cy3 and mRFP fluorescence a 543 nm excitation HeNe laser was used. Phalloidin coupled to Alexa Fluor 647 was imaged using a 633 nm excitation laser. For presentation purposes, images were exported, formatted and brightness adjusted using Fiji ImageJ (Schindelin et al., 2012). The emitted light was monitored between 480–540 nm, 574–625 nm and 650–795 nm, respectively

Spinning disk confocal fluorescence microscopy. For all experiments, cells were mounted inside the StageTop Incubator system (Okolab) on the microscope stage for precise control of the temperature (37°C), humidity (85%), and CO_2-concentration (5%). The spinning disk confocal microscope was equipped with a confocal laser scanning microscope (Nikon Eclipse

Ti) combined with a Confocal Scanner Unit (CSU-W1, Yokogawa). Using an optical beam splitter, the excitation at 488 nm and 561 nm is measured simultaneously and the emitted light was collected between 500-550 nm and 590-650 nm, respectively. Images were acquired with a 100x/1.49 oil immersion objective at 512x512 pixels. The software Andor IQ2 was used for acquisition. For all live-cell time-lapse recordings the exposure time was set to 200 ms and the frame rate to the minimal. The laser power and the number of focal planes (z-frames) were set individually for every measured cell.

Analysis of the colocalization via Manders Overlap Coefficient. Colocalization between two different fluorescent proteins was evaluated using the intensity correlation coefficient-based (ICCB) analysis to evaluate the Manders overlap coefficient embedded in the PlugIn "JACoP" in the ImageJ software (Bolte and Cordelieres, 2006). Here, only the fraction of $Ca_V1.2$–fluorescence overlapping the respective fluorophores in the compartment are reported.

Quantification of cell surface $Ca_V1.2$ and time constant of internalization. The levels of cell surface expression of $Ca_V1.2$ under different pharmacological treatment conditions were estimated by quantifying the fluorescence intensity of the plasma membrane using ImageJ. For each analyzed cell, two regions of interest (ROIs) adjacent to the cell boundary were drawn manually: one around the whole cell including the plasma membrane (whole cell) and a second one at the cell periphery (cell interior), including the cytoplasm of the cell but excluding the cell boundary. The fluorescence of the cell interior, measured as 'integrated density', was subtracted from that of the whole cell to obtain the fluorescence intensity signal at the plasma membrane (surface $Ca_V1.2$). The shown values were normalized to the area of the plasma membrane of each analyzed cell. The time constant of channel internalization was calculated as the decay of fluorescence intensity at the cell surface. Using ImageJ, 6 to 15 ROIs per cell in different z-planes, were drawn manually around fractions of the plasma membrane. The fluorescence in every ROI was measured as 'integrated density' over time, treated as an independent measurement and individually fitted to a mono exponential decay. Scaling and offset parameters from the fits were used to linearly transform each curve, such that all start at 1 and decay to 0. All measurements that yielded nonsensical fit parameters, i.e. negative value for one of the parameters, were excluded from the analysis leaving n = 109 datasets for further investigations. Mean and SD of all the transformed fit lines to the raw data are shown in Figure 3D. The reported time constant was obtained by performing a global fit to a mono-exponential decay to all linearly transformed curves. The uncertainty of the fitted time constant was estimated via bootstrap sampling (Efron and J.Tibshirani, 1993) where 109 (number of ROIs) random samples with replacements are taken from the original set of 109 measurements

and a global fit to this synthetic data was performed. This procedure was repeated 50 000 times and the reported time constant value is given by the mean value and SD of those 50 000 time constants. The bootstrapped time constant distribution and the mean time course of the individual fits to the bootstrap samples are shown in Figure 3E.

Single Molecule Localization Microscopy (SMLM). Fixed HL-1 were washed and permeabilized by incubation in PBS supplemented with 0.5% Triton X-100 for 10 min and blocked for 45 min with 5% normal goat serum (SigmaAldrich) dissolved in PBS. Cells were then incubated for 1 h with the corresponding primary antibody diluted in the same blocking solution followed by several washes with PBS supplemented with 0.1% Tween-20. The cells were incubated with the secondary antibody for detecting tubulin (diluted in blocking buffer), washed twice with PBS supplemented with 0.1% Tween-20 and stored at 4°C until the next day for single molecule localization super-resolution microscopy analysis. Single-molecule localization microscopy data acquisition and analysis was done on our custom-built widefield/TIRF microscope based on an Olympus IX-71 inverted microscope body, as previously described (Stölting et al., 2015). Images were recorded at 80 nm/px in widefield mode with an EMCCD camera (Andor iXon DU897E-C00-#BV) cooled to −75°C. Acquisition was performed at room temperature using imaging buffer (50 mM β−mercaptoethylamine in degassed PBS). Detection of tubulin (Alexa 647) using excitation at 642 nm was followed by measurement of $Ca_V1.2$ (ATTO 488) with excitation at 488 nm. The obtained data was corrected for chromatic aberration. Single molecule localizations were determined from the data using SNSMIL (Tang et al., 2015).

Electrophysiology. Whole-cell patch-clamp technique was used to record calcium currents 24–72 h after cell splitting with a HEKA EPC 10 amplifier using HEKA´s Patchmaster software, as described (Stölting et al., 2015). Recording solutions were as follows: extracellular solution contained in mM: 157 TEA-Cl, 5 $CaCl_2$, 0.5 $MgCl_2$ and 10 HEPES, pH 7.4; internal solution: 125 CsCl, 20 TEA-Cl, 3.6 PCr-Na_2, 10 EGTA, 5 Mg-ATP, 0.2 Na-GTP and 10 HEPES, pH 7.4. HL-1 cells were held at a holding potential of −40 mV and L-type calcium currents were elicited by 100 ms voltage pulses ranging from the holding potential to +60 mV in 10 mV increments.

Statistical Analysis. Statistical analysis and comparisons between the groups were conducted using the GraphPad Prism 5 software. Statistical differences between the data sets were analyzed using One-Way ANOVA followed by post hoc Bonferroni's Multiple Comparison test ($p \leq 0.001$). The data are presented as box plots representing the interquartile range (IQR) with median, 25th and 75th percentile. The whiskers indicate the 95% confidence interval of

the data. Outliers are shown by dots. N is the number of cells given above or below each box in all graphs.

References

Bolte, S., and Cordelieres, F.P. (2006). A guided tour into subcellular colocalization analysis in light microscopy. Journal of microscopy *224*, 213-232.

Efron, B., and Tibshirani, R. J. (1993). An Introduction to the Bootstrap. Monographs on Statistics and Applied Probability. Chapman & Hall/CRC, Boca Raton, Florida, USA.

Guzman, R.E., Miranda-Laferte, E., Franzen, A., and Fahlke, C. (2015). Neuronal ClC-3 Splice Variants Differ in Subcellular Localizations, but Mediate Identical Transport Functions. The Journal of biological chemistry *290*, 25851-25862.

Schindelin, J., Arganda-Carreras, I., Frise, E., Kaynig, V., Longair, M., Pietzsch, T., Preibisch, S., Rueden, C., Saalfeld, S., Schmid, B., Tinevez, J.Y., White, D.J., Hartenstein, V., Eliceiri, K., Tomancak, P., and Cardona, A. (2012). Fiji: an open-source platform for biological-image analysis. Nature methods *9*, 676-682.

Stölting, G., de Oliveira, R.C., Guzman, R.E., Miranda-Laferte, E., Conrad, R., Jordan, N., Schmidt, S., Hendriks, J., Gensch, T., and Hidalgo, P. (2015). Direct interaction of $Ca_V\beta$ with actin up-regulates L-type calcium currents in HL-1 cardiomyocytes. The Journal of biological chemistry *290*, 4561-4572.

Tang, Y., L. Dai, X. Zhang, J. Li, J. Hendriks, X. Fan, N. Gruteser, A. Meisenberg, A. Baumann, A. Katranidis, and T. Gensch. (2015). SNSMIL, a real-time single molecule identification and localization algorithm for super-resolution fluorescence microscopy. *Scientific reports*. 5:11073.